Global Biogeochemical Cycles

RESEARCH ARTICLE
10.1029/2019GB006522

Ge and Si Isotope Behavior During Intense Tropical Weathering and Ecosystem Cycling

J. Jotautas Baronas[1,2], A. Joshua West[1], Kevin W. Burton[3], Douglas E. Hammond[1], Sophie Opfergelt[4], Philip A. E. Pogge von Strandmann[5], Rachael H. James[6], and Olivier J. Rouxel[7]

[1]Department of Earth Sciences, University of Southern California, Los Angeles, CA, USA, [2]Department of Earth Sciences, University of Cambridge, Cambridge, UK, [3]Department of Earth Sciences, Durham University, Durham, UK, [4]Earth and Life Institute, Université catholique de Louvain, Louvain-la-Neuve, Belgium, [5]London Geochemistry and Isotope Centre (LOGIC), Institute of Earth and Planetary Sciences, University College London and Birkbeck, University of London, London, UK, [6]School of Ocean and Earth Science, National Oceanography Centre Southampton, University of Southampton Waterfront Campus, Southampton, UK, [7]IFREMER, Centre de Brest, Unité Géosciences Marines, Plouzané, France

Abstract Chemical weathering of volcanic rocks in warm and humid climates contributes disproportionately to global solute fluxes. Geochemical signatures of solutes and solids formed during this process can help quantify and reconstruct weathering intensity in the past. Here, we measured silicon (Si) and germanium (Ge) isotope ratios of the soils, clays, and fluids from a tropical lowland rainforest in Costa Rica. The bulk topsoil is intensely weathered and isotopically light (mean $\pm 1\sigma$: $\delta^{30}Si = -2.1 \pm 0.3‰$, $\delta^{74}Ge = -0.13 \pm 0.12‰$) compared to the parent rock ($\delta^{30}Si = -0.11 \pm 0.05‰$, $\delta^{74}Ge = 0.59 \pm 0.07‰$). Neoforming clays have even lower values ($\delta^{30}Si = -2.5 \pm 0.2‰$, $\delta^{74}Ge = -0.16 \pm 0.09‰$), demonstrating a whole-system isotopic shift in extremely weathered systems. The lowland streams represent mixing of dilute local fluids ($\delta^{30}Si = 0.2 - 0.6‰$, $\delta^{74}Ge = 2.2 - 2.6‰$) with solute-rich interbasin groundwater ($\delta^{30}Si = 1.0 \pm 0.2‰$, $\delta^{74}Ge = 4.0‰$). Using a Ge-Si isotope mass balance model, we calculate that $91 \pm 9\%$ of Ge released via weathering of lowland soils is sequestered by neoforming clays, $9 \pm 9\%$ by vegetation, and only $0.2 \pm 0.2\%$ remains dissolved. Vegetation plays an important role in the Si cycle, directly sequestering $39 \pm 14\%$ of released Si and enhancing clay neoformation in surface soils via the addition of amorphous phytolith silica. Globally, volcanic soil $\delta^{74}Ge$ closely tracks the depletion of Ge by chemical weathering (τ_{Ge}), whereas $\delta^{30}Si$ and Ge/Si both reflect the loss of Si (τ_{Si}). Because of the different chemical mobilities of Ge and Si, a $\delta^{74}Ge$-$\delta^{30}Si$ multiproxy system is sensitive to a wider range of weathering intensities than each isotopic system in isolation.

Key Points:
- Very low Ge and Si isotope ratios in clays and bulk soils reflect intense chemical weathering
- Si cycling is strongly influenced by vegetation in extremely weathered soils
- In global volcanic soils, Si isotopes and Ge/Si reflect Si loss, while Ge isotopes reflect Ge loss

Supporting Information:
- Table S1

Correspondence to:
J. J. Baronas,
jotautas.baronas@gmail.com

Citation:
Baronas, J. J., West, A. J., Burton, K. W., Hammond, D. E., Opfergelt, S., Pogge von Strandmann, P. A. E., et al. (2020). Ge and Si isotope behavior during intense tropical weathering and ecosystem cycling. *Global Biogeochemical Cycles*, *34*, e2019GB006522. https://doi.org/10.1029/2019GB006522

Received 29 DEC 2019
Accepted 23 JUL 2020
Accepted article online 3 AUG 2020

1. Introduction

Physical and chemical interaction of water, rocks, and biota takes place in the critical zone—the Earth surface environment extending from the tree canopy to the bedrock. This interaction shapes the land surface, supplies dissolved nutrients and trace elements to terrestrial and marine ecosystems, and modulates climate via the consumption of atmospheric CO_2 (e.g., Frings & Buss, 2019). The latter process, which relies on the chemical weathering of silicate rocks, has been proposed as a major mechanism stabilizing (Berner et al., 1983; Walker et al., 1981) or perturbing (Macdonald et al., 2019; Raymo & Ruddiman, 1992) climate at different stages of Earth history. Testing these hypotheses requires the reconstruction of silicate weathering over geological timescales. Although there are currently no methods that can reliably reconstruct absolute chemical weathering fluxes in the past, the relative intensity of chemical weathering is to some degree reflected in records of ocean chemistry (Froelich et al., 1992; Hathorne & James, 2006; Li & Elderfield, 2013; Misra & Froelich, 2012) and in the geochemical signatures of secondary weathering phases formed in soils (e.g., Amundson, 2013; Bouchez et al., 2013). A robust understanding of how elemental and isotopic proxy signatures are generated in the weathering environment is needed to interpret these geological sedimentary records.

The chemical weathering of silicate rocks releases constituent elements to solution, with variable fractions of each element retained in secondary weathering phases, such as aluminosilicate clays and refractory oxides.

The formation of such phases often results in the fractionation of element ratios due to differing stoichiometry and thermodynamic properties of the dissolving and precipitating phases. Secondary phase formation also results in the fractionation of isotope ratios due to kinetic (e.g., Watkins et al., 2017) and quantum vibrational effects (e.g., Blanchard et al., 2017). Under conditions of limited erosion and continued chemical weathering (e.g., in humid tropical environments), primary phases become depleted and secondary phases can then become thermodynamically destabilized. This results in further chemical and isotopic fractionation as secondary phases transform into new clay minerals and oxides (a process referred to as neoformation). Over thousand-year and longer timescales, this fractionation results in preferential loss of certain elements and isotopes from the critical zone, with the remaining solids containing a record of the long-term weathering intensity.

Several geochemical proxies of silicate weathering intensity have been investigated, most notably germanium to silicon (Ge/Si) ratios (Froelich et al., 1992; Kurtz et al., 2002; Lugolobi et al., 2010; Murnane & Stallard, 1990), lithium isotope ratios (e.g., Dellinger et al., 2015; Hathorne & James, 2006; Misra & Froelich, 2012; Pogge von Strandmann & Henderson, 2015), and silicon isotope ratios (e.g., Frings et al., 2016; Georg et al., 2006a; Ziegler et al., 2005) in both the dissolved and the solid products of weathering. Recently, germanium isotopes have also been shown to trace chemical weathering of silicates (Baronas et al., 2017, 2018). However, each elemental or isotopic proxy reflects a multitude of processes in the critical zone and—if reconstructions are based on marine records—in the ocean, resulting in a range of possible interpretations of each proxy record (e.g., Baronas et al., 2017; Frings et al., 2016; Hammond et al., 2004; Li & West, 2014).

Germanium is a trace element that is chemically similar to Si, and in the critical zone, both elements are primarily sourced from silicate rocks that exhibit Ge/Si ratios in the range of 1–3 μmol/mol (Bernstein, 1985; De Argollo & Schilling, 1978; Mortlock & Froelich, 1987). During the precipitation of secondary phases associated with weathering, dissolved Ge is removed from solution preferentially over dissolved Si, resulting in natural waters with Ge/Si ratios of 0.1–3 μmol/mol (Anders et al., 2003; Baronas et al., 2017, 2018; Froelich et al., 1985, 1992; Kurtz et al., 2002, 2011; Lugolobi et al., 2010; Meek et al., 2016; Mortlock & Froelich, 1987; Murnane & Stallard, 1990). Similarly, Si isotope ratios (δ^{30}Si) are fractionated during the formation of secondary weathering solids which preferentially incorporate lighter Si isotopes ($\delta^{30}\mathrm{Si} = -3$ to 0‰), leaving the corresponding soil waters and streams isotopically heavy ($\delta^{30}\mathrm{Si} = 0$ to 3‰) relative to primary silicates ($\delta^{30}\mathrm{Si} \approx -0.3$ to 0‰) (e.g., Frings et al., 2016; Georg et al., 2007; Opfergelt & Delmelle, 2012; Ziegler et al., 2005). In addition, terrestrial vegetation can incorporate significant amounts of soil water Si (primarily storing this Si in amorphous silica phytoliths), again preferentially removing light isotopes (e.g., Ding et al., 2005; Opfergelt & Delmelle, 2012; Opfergelt et al., 2006). In contrast, most plants discriminate against Ge, and as a result, the phytoliths exhibit low Ge/Si values (Blecker et al., 2007; Derry et al., 2005; Lugolobi et al., 2010; Meek et al., 2016; Sparks et al., 2010), elevating Ge/Si in the remaining soil water pool. The combined use of δ^{30}Si and Ge/Si therefore allows evaluation of the ecosystem influence on the local Si cycle, both at the soil profile scale (Cornelis et al., 2010, 2014; Lugolobi et al., 2010; Opfergelt et al., 2010; White et al., 2012) and at the catchment scale (Baronas et al., 2018).

Two recent studies have shown that Ge isotopes behave similarly to Si during weathering, with fluids enriched ($\delta^{74}\mathrm{Ge} = 0.9$ to 5.5‰; Baronas et al., 2018) and weathered solids depleted in heavy isotopes ($\delta^{74}\mathrm{Ge} = -0.1$ to 0.6‰; Qi et al., 2019) relative to primary igneous silicates ($\delta^{74}\mathrm{Ge} = 0.4$ to 0.8‰; Rouxel & Luais, 2017). However, Ge isotopes are a very recent addition to the weathering proxy toolbox, and while these studies have established the broad first-order systematics of δ^{74}Ge, more work is needed to understand the mechanistic controls on this proxy and its potential to trace different critical zone processes.

Over geological timescales, the heavy signatures of isotopic systems like δ^{30}Si and δ^{74}Ge in continental fluids can only be maintained if the isotopically light secondary solids are continuously eroded from the continents (Bouchez et al., 2013). When chemical weathering rates outpace erosion, secondary phases accumulate and soils develop. With enough time, and especially in tropical climates, this can result in extremely thick and weathered soils that effectively isolate surface waters from the underlying parent rock, resulting in systems where chemical weathering is limited by the supply of fresh primary minerals (Stallard & Edmond, 1983; West et al., 2005). It has been shown that in such extremely erosion-limited regimes, the continued chemical weathering of soils can result in progressive depletion of ^{30}Si, driving all soil materials and weathering fluids

towards lower δ^{30}Si (Opfergelt et al., 2012; Ziegler et al., 2005). There are currently, however, very few detailed systematic studies of Si (and even more so Ge) isotope behavior in such environments characterized by extremely high-intensity weathering.

In this study, we have investigated Ge/Si, δ^{30}Si, and δ^{74}Ge distributions in the groundwaters, streams, and deeply weathered volcanic soils of a tropical rainforest in Costa Rica, to better understand how these proxies reflect intense tropical chemical weathering and other critical zone processes locally and globally.

2. Methods

2.1. Site Description

The study site is located primarily within the La Selva Biological Station of the Organization for Tropical Studies (OTS) in the Atlantic lowlands of Costa Rica, 35 km northeast of Barva Volcano (Figure 1). The elevation ranges from 20 to 140 m above sea level. Rainfall averages 4 m/year and is relatively constant in May through November (300–500 mm/month), with a minimum of 150–160 mm in January–February (Genereux & Jordan, 2006). The mean annual temperature is 24–26°C and is relatively constant throughout the year (Sanford et al., 1994). The warm and wet climate supports a tropical rainforest ecosystem.

The parent rock primarily consists of a series of >1.2 My old andesitic plagioclase-rich lava flows (Alvarado Induni, 1990; McDade et al., 1994a). The study area is underlain by >20 m thick, strongly weathered soils, developed on top of the lava flows, as well as alluvial Holocene–Pleistocene deposits at the lowest elevations along the Rio Sarapiqui and Rio Puerto Viejo rivers. These alluvial deposits are sourced from the same andesitic parent material that underlies the rest of the study region, and the deposits are also covered by thick, highly weathered soils. The mineralogy of bulk soils from La Selva has been described in detail previously by Kleber et al. (2007). Briefly, the soils are classified as Oxisols and are primarily composed of gibbsite and various forms of halloysite-kaolinite, with smaller amounts of goethite and hematite. Trace amounts of quartz and magnetite are also present. Soil profiles show evidence of active mineralogical transformations of clays and oxides.

2.2. Sample Collection

Samples were collected from the La Selva Biological Station and neighboring areas between 14 and 20 May 2010. Most samples were collected from streams within the Biological Station, accessed by foot using the station trail network. Additional samples (prefix CR) were collected from different sites along the Sarapiqui River draining the wider region, accessed by road. Guacimo Spring, discharging about 1 km southwest of the study area, was also sampled, as it reflects the composition of volcanic interbasin groundwater (IBGW), recharged at higher elevations on the slopes of Barva Volcano (e.g., Genereux et al., 2009). The importance of volcanic IBGW to the water budgets of some catchments in the La Selva Biological Station has been demonstrated by a number of studies over the years (Genereux, 2004; Genereux & Jordan, 2006; Genereux & Pringle, 1997; Genereux et al., 2005, 2009; Pringle, 1991; Pringle et al., 1990; Wiegand & Schwendenmann, 2013).

The Taconazo and Arboleda streams were sampled twice, on 14th (LS-01 and LS-02, respectively) and 19th (LS-12 and LS-13, respectively) of May, just upstream of gauged V-notch weirs, where discharge is measured every 15 min. During this time period, the discharge of both streams remained relatively stable with a baseflow of 17–22 and 175–185 L/s at Taconazo and Arboleda, respectively, and briefly rising to 37 and 215 L/s, respectively, during two minor rain events on May 15th. The significantly higher discharge at Arboleda is partly due to its larger catchment area (0.50 km^2 compared to Taconazo's 0.26 km^2) but primarily due to the high contribution of IBGW sourced from outside the catchment (Genereux et al., 2005). The flow regime of both streams during our sampling period was very close to the long-term mean discharge, which was 21 L/s for Taconazo and 193 L/s for Arboleda during the period of 2006–2010 (data downloaded from https://anetium.ots.ac.cr, collected by the Office of Tropical Studies, under the direction of D. Genereux). Given the small overall study area (15 km^2), we expect the flow regime to be similar in all other La Selva streams sampled in this study. The discharge of the Sarapiqui River was not measured but is considerably higher than any of the streams within the La Selva Station.

Stream and river water samples were collected in prerinsed 15-L collapsible plastic containers and transported directly back to the laboratory at the La Selva Biological Station. Groundwaters were collected from existing shallow (<1 m deep) wells at La Selva (Genereux et al., 2005) using a plastic bailer. Temperature,

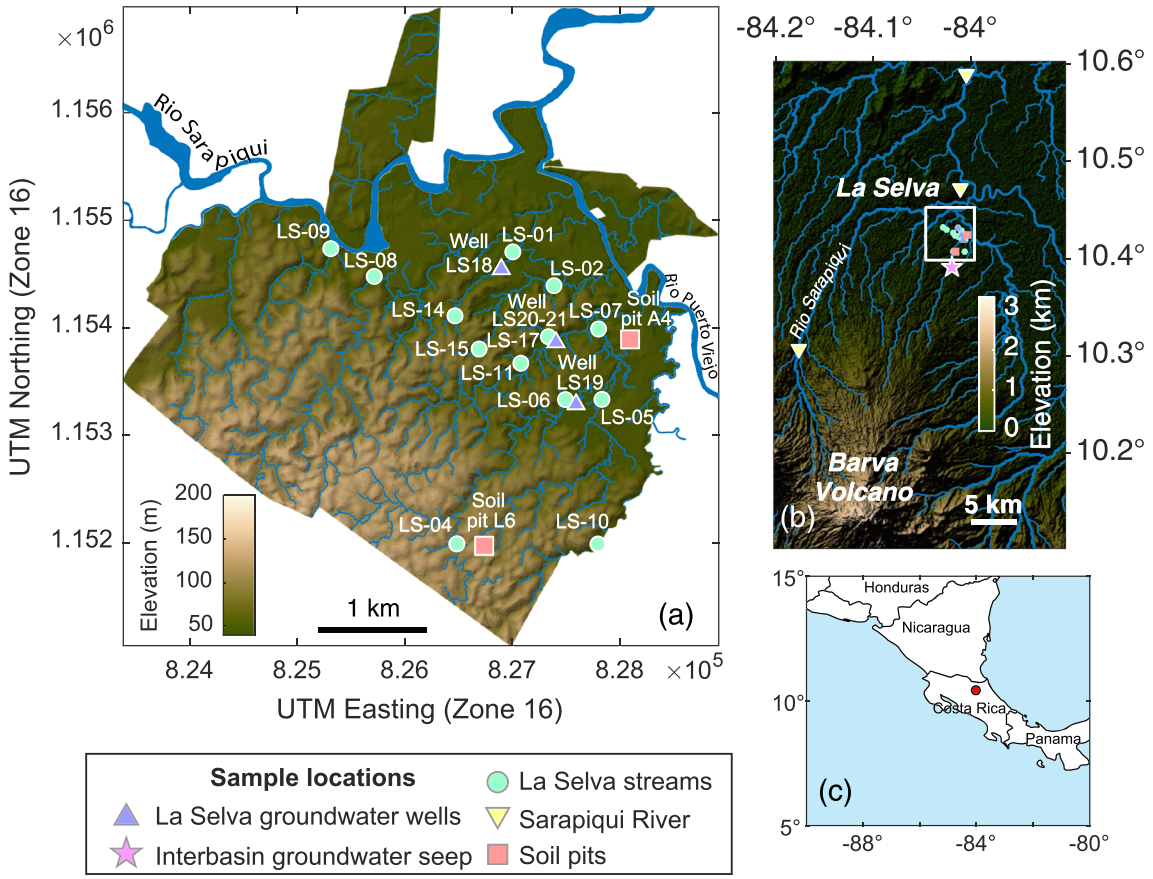

Figure 1. Map of the study site, showing sample locations in the La Selva Biological Station (a), the regional setting, including the nearby Barva Volcano (b), and the setting within Central America (c). Stream sample locations are shown as cyan circles, sampled wells as purple triangles, and soil pits as red squares. In panel (b), the interbasin groundwater sample (CR5) that was collected at the Guacimo Spring is shown as a pink star and the samples of the large Sarapiqui River are shown as yellow triangles.

pH, and conductivity were measured in situ using a handheld meter, with pH calibrated daily using pH buffers. All water samples were immediately (typically within 1 h) filtered through 142-mm diameter, 0.2-μm polyethersulfone (PES) membrane filters using a peristaltic pump and an inline Sartorious PFA filter holder. The filtration apparatus was cleaned between each sample and prerinsed with sample before collecting filtrate. For the analyses reported in this study, three aliquots of filtrate were collected into separate low-density polyethylene (LDPE) bottles. One bottle was filled completely and left unpreserved, for analysis of anion concentrations. The other bottle was acidified with quartz-distilled HNO_3 to pH < 2, for cation, Ge concentration, and Si isotope ratio analyses conducted in this study. A third, larger, 500- to 1,000-ml aliquot was also acidified and used for Ge isotope analysis. Alkalinity was measured using Gran titration on a separate unfiltered water aliquot.

Filter papers were stored in plastic bags and returned to the University of Oxford, UK, where suspended sediment was removed with a spatula and dried at 60°C. A small amount of fine-grained material could not be removed from the filter papers, but this small proportion is not expected to bias analysis of suspended sediment composition. Sediment from the stream bed was collected at selected sites in plastic bags and dried at 60°C (referred to as "bedload" samples). Since bedrock exposures are not present at La Selva or in the immediately surrounding area, visibly well-preserved rock cobbles were collected from selected stream sites and analyzed after removing any potentially altered outer surfaces to provide a representative sampling of parent rock.

Soils were collected from two soil pits (originally 3- to 4-m depth) dug in 1997 at the La Selva "Carbono" plots (Clark & Clark, 2000; Kleber et al., 2007; Veldkamp et al., 2003). Soil pit IDs were adopted from the previous

plot naming conventions, with samples collected from the same two pits (A4 and L6) that were studied in detail for mineralogical composition by Kleber et al. (2007). Pit A4 reflects "old alluvial" soil developed on a river terrace probably of Pleistocene age, while L6 is "residual" soil developed on ~1.2 Ma lava flows (Veldkamp et al., 2003). Both are deeply weathered Oxisols, with similar andesitic parent material, despite the difference in the mode and age of initial deposition (Kleber et al., 2007). Soils were collected from the exposed pit walls. Since some additional weathering had occurred since the pits were dug, ~50 cm was excavated into the side of the pit wall before collecting samples into plastic bags with a hand trowel. Clay fractions (operationally defined as the <2 μm particle size fraction) were separated from selected solid samples (including soils and stream bed sediment) by settling in deionized water after sonication and dispersion by addition of a sodium phosphate salt.

To collect soil pore waters, rhizon samplers (10-cm length, 2.0-mm diameter, 0.15-μm pore size PES) were inserted horizontally into the excavated surface of the pit walls. Syringes were left to fill for ~24 h before dispensing the collected pore waters into prewashed 30-ml PP bottles. Plant samples were collected from understory vegetation, selecting a single individual from species that appeared to be visibly common in the area around each soil pit. Species were not formally identified but based on the appearance were likely seedlings or shrubs belonging to the Arecaceae family, that is, palms (Figure S1). A thorough description of different vegetation types and species abundances at La Selva is given by McDade et al. (1994b). Samples of mature leaves were cut and collected in a plastic bag, transported to the laboratory, cleaned with deionized water in a sonicating bath, and dried before grinding and ashing for analysis. All water, sediment, and soil samples were refrigerated following collection, except during the air transport (~24 h) from Costa Rica to Oxford, UK.

2.3. Major and Trace Element Analyses

Solid samples were powdered using a mortar and pestle and dissolved in a HF/HNO_3 mixture in Teflon vials at 90°C. Solutions were evaporated to dryness and residual salts dissolved in 2% HNO_3 for analysis by ICP-MS (Thermo Scientific X-Series II) at the University of Southampton, UK. Measurements were checked against four certified rock reference materials (JGb-1, JB-1a, JA-2, and MAG-1) and the reproducibility of the analyses was better than ±3% for all elements. Measured concentrations were within ±5% of the certified or recommended values for all elements except K (±10%). Si concentrations in solids were measured after NaOH fusion, as described below. Si measurement accuracy of solids was ±10%, as confirmed by analyses of three certified rock reference materials (BIR-1, DTS-1, and SCO-1).

The untreated aliquot of each water sample was analyzed for major anions (Cl^- and SO_4^{2-}) by ion chromatography at the University of Southern California, USA, using a Metrohm IC 850 equipped with an A4/150 anion exchange column with conductivity suppression, using a 3.2-mM Na_2CO_3/1.0-mM $NaHCO_3$ eluent with a flow rate of 0.7 ml/min. Conductivity signals were calibrated against a series of standards prior to the analytical session. A certified reference material (ION-915, Environment Canada) was run after every 10–15 samples. All analyses were within the range of certified values, and replicate analyses were within 10% (2σ).

Other major and trace elements, including Ca, Mg, Na, K, Sr, Al, and Fe, were measured on the acidified portion of each water sample using a Thermo Element2 ICP-MS (inductively coupled plasma mass spectrometer) at the University of Oxford. All elements were analyzed in low-resolution mode. Intensities for trace elements were calibrated using multiple dilutions of an in-house standard solution with a composition similar to average river water. Major elements were calibrated using dilutions of the TROIS-94 certified reference water (Trois Riviers, Environment Canada). Indium was used as an internal standard to correct for signal drift during the analytical session. All analyses were within the range of certified values, and replicate analyses were within 10% (2σ). Charge balance was within 20% for all but one sample (LS06) and was within 5% for most samples. Dissolved Si concentrations were measured by spectrophotometry using the molybdate blue method with citric and amino acid reagents.

2.4. Germanium Concentration Analysis

Dissolved Ge concentrations in water samples were measured using isotope dilution-hydride generation ICP-MS based on the method developed by Mortlock and Froelich (1996), as modified by Baronas et al. (2016). Briefly, a monoisotopic ^{70}Ge spike was added to 5 ml of sample gravimetrically and the sample

diluted to 20 ml with 0.01-M distilled HCl. Dissolved Ge was converted to hydride by reacting with $NaBH_4$, and the resulting GeH_4 gas was preconcentrated on a liquid N_2 trap prior to being injected into a Thermo Element 2 ICP-MS instrument at the University of Southern California. Ge concentrations in solid samples were determined using MC-ICP-MS, after double spiking, digestion, and chromatographic separation for δ^{74}Ge analysis, as described below. Ge concentration in each sample was determined based on the measured $^{70}Ge/^{74}Ge$ ratio.

2.5. Silicon Isotope Analysis

2.5.1. Fusion of Solids

Solid samples, including vegetation, were digested using a fusion procedure following Georg et al. (2006b). Twenty milligrams of finely powdered sample were fused with ~200 mg high-purity NaOH in silver crucibles at 720°C for 10 min. The crucibles with fusion cakes were sonicated for 30 min in 20-ml doubly deionized water (DDIW) and left to dissolve for 24 h. The solution was then transferred into 250-ml polyethylene bottles, carefully rinsing to ensure complete recovery, diluted to 200–250 ml with DDIW, and acidified with 3-ml trace metal grade concentrated HNO_3. Vegetation samples were additionally ashed in Pt crucibles at 450°C prior to fusion.

2.5.2. Cation Exchange Chromatographic Separation

Si isotope analyses followed the approach of Georg et al. (2006b). Si was separated from sample matrix by ion exchange chromatography. A 10-ml column was filled with 1.8-ml wet volume BioRad AG50W-X12 (200–400 mesh) resin. The column was washed with a full column volume of DDIW, followed by a sequence of 3M-6M-10M-6M-3M HCl (full column volume of each), and then preconditioning with three column volumes of DDIW. Samples (volumes ranging from 0.05 to ~3 ml) were then loaded onto the column in a ~1% HNO_3 matrix and eluted with 2- to 5-ml DDIW to obtain a final solution of 0.5 ppm Si (yielding about ~8 V [80 pA] for ^{28}Si during analysis). All bracketing standard and reference material aliquots were purified using the same cation exchange method as the samples. Reference materials (Diatomite, BHVO-2, and Merck Quartz) were processed with the same method. Larger batches of NBS-28 were prepared by eluting with up to 20-ml DDIW.

2.5.3. MC-ICP-MS

Following chromatographic separation of Si, isotope ratios were measured using a Nu Plasma II HR-MC-ICP-MS at the University of Oxford in medium-resolution mode, on the flat part of the peak shoulder to avoid $^{14}N^{16}O^+$ interference on ^{30}Si. For each sample, ratios were measured over 25 integrations of 10 s, repeated in five blocks. For each block, the sample analysis was bracketed by measurement of concentration-matched NBS-28 standard solution which had passed through the same column chromatography procedure as the samples. δ^{30}Si values are reported in ‰ as $^{30}Si/^{28}Si$ sample ratio normalized to the average $^{30}Si/^{28}Si$ ratio of bracketing NBS-28 measurements. The measurement uncertainty is reported as the internal 2σ standard error of sample replicates, or 2σ standard deviation (SD) of all NBS-28 bracketing standard measurements within a given analytical session, whichever is higher. Reference materials (diatomite, BHVO-2, and Merck Quartz) were analyzed during sample runs, yielding values of 1.35 ± 0.16‰ (mean ± 2 SD; $n = 6$), -0.28 ± 0.14‰ ($n = 5$), and -0.01 ± 0.04‰ ($n = 3$), respectively, all within the ranges reported in previous studies (Abraham et al., 2008; Georg et al., 2009; Reynolds et al., 2007). Comparison of measured $^{30}Si/^{28}Si$ and $^{29}Si/^{28}Si$ ratios indicates good correlation with a slope close to that expected for mass-dependent fractionation (Table S1).

2.6. Germanium Isotope Analysis

2.6.1. River Water

Filtered river water (0.5 to 1.0 L) containing 6–18 ng of Ge was acidified with distilled HNO_3 and spiked with a Ge isotope double spike ($^{73}Ge/^{70}Ge \approx 1$, previously calibrated and used by Escoube et al., 2012, 2015 and Baronas et al., 2018, 2019). The spike/sample Ge mass ratio ranged between 1 and 2, and a purified dissolved $FeCl_3$ salt was added to obtain an Fe concentration of ~0.2 mmol/L. The samples were well mixed and allowed to equilibrate for at least 16 h. Next, $Fe(OH)_3$ flock was precipitated by adding Optima-grade NH_4OH until the solution reached a pH of 8–10. The flock was collected by settling and centrifugation, redissolved in 2-ml concentrated Teflon-distilled HNO_3 and diluted to 10 ml with DDIW. The samples were then dried, redissolved in 1-ml concentrated Optima-grade HF, and diluted to 30 ml with DDIW to obtain a final

1M HF solution. The samples were then purified through anion exchange columns as described below. The full procedural blank was determined by processing spiked DDIW and ranged from 0.01 to 0.3 ng Ge.

2.6.2. Rocks and Sediments

A method adapted from Rouxel et al. (2006) was used for solid sample digestion. Dried ground sample (10–130 mg) containing 30–300 ng of Ge was weighed into Teflon digestion vessels and spiked with a Ge isotope double spike ($^{73}Ge/^{70}Ge \approx 1$) in a spike/sample Ge mass ratio between 1 and 2. The samples were digested by adding 10-ml concentrated Teflon-distilled HNO_3 and heating in a pressurized Teflon vessel at 90°C for 48 h. Then, to ensure the oxidation of any organic matter, 1 ml of Optima-grade H_2O_2 was added and digests were heated uncapped at 70°C until dry. After cooling, 4-ml DDIW and 1-ml concentrated Optima-grade HF were added and samples were digested at 70°C for 48 h. Replicate digestions done without H_2O_2 yielded the same results, indicating that the presence of organic matter does not interfere with Ge digestion. After cooling, the samples were diluted to 30 ml with DDIW to obtain a final 1M HF solution that was purified through anion exchange columns as described below. The full procedural blank was determined by processing only the Ge double spike and was below 1.7 ng Ge.

2.6.3. Anion Exchange Chromatographic Separation

A procedure adapted from Rouxel et al. (2006) was used. All reagents used were either in-house Teflon distilled or Optima grade. A 10-ml column was loaded with 1.8 ml (wet volume) of BioRad AG1-X8 resin, washed with 10-ml aliquots of 3M HNO_3, 0.28M HNO_3, and DDIW each, then conditioned with 5-ml 1M HF. Samples in 1M HF solution prepared as above were centrifuged to separate insoluble fluorides. The presence or amount of insoluble fluorides at this stage did not appear to affect the final Ge recovery. Ten to 29 ml of the solution was carefully added to columns. The remaining matrix was eluted with 5 ml of 1M HF followed by 3 ml of DDIW, while fluorinated Ge was retained on the column. Ge was then eluted with 10-ml 0.28M HNO_3. If required, the solution was dried down and redissolved in a smaller volume of 0.28M HNO_3 to obtain the 2–10 ppb Ge concentration required for isotope measurements. Each column was reused 4–5 times, except when retention of organic compounds from the previous sample was observed based on the color, in which case the resin was replaced. Ge blanks from reused resin were below detection limit. Ge recovery ranged from 50% to 100%, with loss most likely during the coprecipitation or digestion steps for the fluid and solid samples, respectively. Incomplete recovery does not affect the measured $\delta^{74}Ge$ values, as all samples were double spiked prior to sample preparation. Accuracy was confirmed by analyses of certified reference materials BIR-1 and DTS-1 ($\delta^{74}Ge = 0.62 \pm 0.24$ and 0.61 ± 0.07 [$n = 2$; 2σ], respectively), which had recovery between 60% to 90% similar to other samples and agreed well with previously measured values (Escoube et al., 2012). Double spike calculations also showed no difference between the full procedural fractionation factors (F_{inst}, including fractionation in the ICP instrument; see Siebert et al., 2001) of the pure NIST standard and the samples with incomplete recovery.

2.6.4. HG-MC-ICP-MS

Ge isotope analyses were performed on a Thermo Neptune multicollector ICP-MS at Ifremer (Brest, France) using a method adapted from Guillermic et al. (2017). Sample solutions of 2–10 ppb natural Ge in 0.28M HNO_3 were introduced into an online hydride generation system (CETAC HGX-200) at a rate of 150 µl/min where they were mixed with $NaBH_4$ solution introduced at an equal rate. The dissolved $Ge(OH)_4$ species were reduced to gaseous GeH_4 and transported into the ICP-MS torch using Ar carrier gas. The Neptune MC-ICP-MS was operated in low mass resolution mode, measuring ^{70}Ge, ^{72}Ge, ^{73}Ge, and ^{74}Ge in L2, C, H1, and H2 cups, respectively. In addition, L4, L3, L1, and H4 cups were also monitored for ^{68}Zn (possible interference as ^{70}Zn), ^{69}Ga, ^{71}Ga (possible interferences at m/z 70), and ^{77}Se (possible interference as ^{74}Se), respectively. No interferences were detected in any of the runs, and therefore, no corrections were necessary. The samples were bracketed using a NIST-3120a standard solution that had a total Ge concentration generally within ~20% of the bracketed sample and was double spiked to have a spike/sample ratio within ~20% of the bracketed sample. Each sample or standard run consisted of six measurement blocks each lasting 2 min (30 cycles of 4 s each), and in most cases, four to five blocks displaying the most stable signal were retained. Therefore, each measurement represents 8–10 min of counting statistics at signal intensities ranging from 0.4 to 6 V (4–60 pA) at ^{74}Ge (depending on Ge concentration in sample solution, instrument tuning, and freshness of the $NaBH_4$ solution). The $\delta^{74}Ge$ values are calculated for each block using the double-spike data reduction routine of Siebert et al. (2001) and are reported in ‰ as $^{74}Ge/^{70}Ge$ sample ratio normalized to the average $^{74}Ge/^{70}Ge$ ratio of bracketing NIST 3120a measurements. This method also yields

Ge concentration values based on the measured spike/sample ratio. Instrumental blank measurements were generally below 2% of measured sample and standard intensities, suggesting that a washout time of 8 min was sufficient to avoid significant memory effects. The measurement uncertainty is reported as the internal 2σ standard error of the used sample blocks, or 2σ SD of all NIST 3120a bracketing standard measurements within a given analytical session, whichever is higher. To confirm accuracy, a number of standard reference materials were digested, chromatographically separated, and analyzed alongside samples, as reported previously by Baronas et al. (2018). Analyses of reference materials yielded values that agree well with previous literature (δ^{74}Ge of 0.58 ± 0.06‰ for DTS-1, 0.53 ± 0.08‰ for BIR-1, and 0.55 ± 0.15‰ for BHVO-1).

3. Results

3.1. Soil and Clay Chemistry and Mineralogy

The local andesite rock, based on the analysis of the visibly least-altered stream bed cobbles considered representative of parent rock, is composed of ~50–60 wt% SiO_2, 15 wt% Al_2O_3, 6–10 wt% Fe_2O_3, and other major oxides ranging between 1 to 8 wt% each (Table 1 and Figure S2). Relative to this parent rock, the bulk soils and separated clays sampled at two soil pits are strongly desilicified (20–28 wt% SiO_2), enriched in Al_2O_3 (27–35 wt%) and Fe_2O_3 (15–18 wt%), and strongly depleted in all major cations (<1 wt% of Na_2O, K_2O, CaO, and MgO). There are no significant differences between the two soil pits (A4 and L6). These results are consistent with previous studies, which identified the strongly weathered character of these soils, with clay-sized fraction between 67% and 83% and relatively invariant in the top 2 m (Kautz & Ryan, 2003; Kleber et al., 2007). In terms of major oxide chemistry, the separated clays are chemically indistinguishable from bulk soils (Table 1 and Figure S2). Using qualitative powder XRD (Proto AXRD at the Natural History Museum of Los Angeles), the major mineral phases were found to be gibbsite, kaolinite/halloysite, and goethite, as well as traces of magnetite (data not shown). These results are consistent with a previous study of soil mineralogy at these sites (Kleber et al., 2007). There are no distinguishable differences in mineralogy between separated clay size fraction and bulk soils, except that a small amount of residual quartz was present in the bulk soil samples but not in the clay fraction.

To quantify the degree of soil alteration by chemical weathering, we employ the widely used mass transfer coefficient (τ value) approach (Brimhall & Dietrich, 1987; Chadwick et al., 1990; Nesbitt, 1979), where the concentration of the element of interest is normalized to another element that is not solubilized to any significant degree during chemical weathering. We tested both Zr and Ti as potential immobile elements. While they yielded similar values, the use of Ti resulted in lower uncertainties due its more homogeneous distribution in parent rock samples (Text S1). We thus only discuss Ti-normalized values below (both sets of τ values for all elements are given in Table S2). Using Ti also allows us to compare our results with the bulk soil data published by Kleber et al. (2007), which goes down to 400-cm depth and provides values in good agreement with our results at the depths sampled in both studies (Figure 2).

The La Selva soils are almost completely depleted of Na, K, Ca, and Mg, generally with $\tau < -0.95$ and only a slight increase towards the surface horizon (Table S2). The loss of Si is less extensive ($\tau_{Si} \approx -0.8$) and relatively invariant with depth (Figure 2a). Ge shows lower degree of depletion than Si ($\tau_{Ge} \approx -0.2 \text{to} -0.5$, Figure 2b). In contrast, Fe has been fully retained ($\tau_{Fe} \approx 0$) and Al is even slightly enriched in the 50–300 cm horizon (Figure 2c). The τ values calculated for bulk soils and clays separated via settling are indistinguishable for most elements, including Si (Figure 2a). The exceptions include τ_{Al} and τ_{Ge}, which show significant enrichment relative to bulk soils (Figures 2b and 2c). It is theoretically possible that increase in clay τ values results from the preferential loss of some heavy Ti-bearing phases (such as rutile or titanite) during the clay separation procedure. However, in this case, the increase in clay τ values would be expected for all elements, which is not the case (Table S2). We therefore interpret and discuss the difference between soil and clay τ values as reflective of ongoing weathering processes (section 4.3.2).

3.2. Fluid Chemistry

Major and trace element concentrations in La Selva streams and groundwater seeps span a wide range of values (Table 2). Local rainwater reflects seawater aerosol inputs (Na and Cl concentrations of ~60 μmol/L, close to long-term average; Eklund et al., 1997), whereas Ge and Si concentrations are low (4 μmol/L and 9 pmol/L, respectively) with Ge/Si of 2.3 μmol/mol. Samples of soil pore water and shallow

Global Biogeochemical Cycles

10.1029/2019GB006522

Table 1
Chemical Composition of Solids Sampled at La Selva Biological Station

Sample	Depth (cm)	ID	Al_2O_3 (wt%)	Fe_2O_3 (wt%)	SiO_2 (wt%)	Na_2O (wt%)	K_2O (wt%)	CaO (wt%)	MgO (wt%)	MnO (wt%)	TiO_2 (wt%)	Th (μg/g)	Zr (μg/g)	Ge (μg/g)	Ge/Si (μmol/mol)	$\delta^{30}Si$ (‰)	$\delta^{74}Ge$ (‰)
Parent rock																	
Rock 1	–	LS-R1	14.1	5.7	61.7	4.00	3.61	3.97	1.72	0.14	1.03	16.6	311	1.54	2.07	−0.13 ± 0.18	0.64 ± 0.08
Rock 2	–	LS-R2	14.1	9.3	53.8	2.43	1.25	8.30	5.73	0.15	1.12	4.8	120	1.52	2.34	−0.09 ± 0.25	0.54 ± 0.02
Bulk soils																	
Soil pit A4	0	A4-0-B	27.1	15.2	20.9	0.05	0.26	0.17	0.36	0.11	2.02	13.2	282	1.55	6.16	−1.74 ± 0.21	−0.22 ± 0.15
Soil pit A4	50	A4-50-B	35.1	17.1	27.1	0.04	0.25	0.03	0.29	0.19	2.19	16.6	342	–	–	−2.11 ± 0.23	–
Soil pit A4	100	A4-100-B	–	–	–	–	–	–	–	–	–	–	–	1.87	6.00	–	−0.16 ± 0.08
Soil pit A4	200	A4-200-B	34.2	18.3	28.4	0.03	0.13	0.02	0.24	0.08	2.39	17.5	368	2.22	6.48	−1.88 ± 0.16	−0.08 ± 0.08
Soil pit L6	0	L6-0-B	31.1	17.4	21.3	0.05	0.18	0.06	0.32	0.04	2.00	13.6	284	1.63	6.33	−2.05 ± 0.19	−0.28 ± 0.27
Soil pit L6	50	L6-50-B	34.8	17.9	25.7	0.03	0.15	0.02	0.26	0.04	2.05	15.0	306	1.95	6.30	−2.19 ± 0.18	−0.08 ± 0.08
Soil pit L6	200	L6-200-B	31.1	15.8	25.9	0.02	0.13	0.01	0.18	0.03	1.82	15.3	287	2.08	6.63	−2.47 ± 0.25	0.07 ± 0.04
Separated clays																	
Soil pit A4	0	A4-0-C	32.9	15.7	22.4	0.08	0.62	0.23	0.27	0.13	1.66	14.7	299	1.95	7.21	−2.60 ± 0.23	−0.27 ± 0.05
Soil pit A4	200	A4-200-C	34.7	16.5	27.3	1.31	0.12	0.02	0.18	0.06	1.94	19.0	356	2.56	7.76	−2.44 ± 0.07	−0.06 ± 0.08
Soil pit L6	0	L6-0-C	32.9	17.1	23.3	0.09	0.25	0.06	0.21	0.03	1.77	15.0	307	2.16	7.69	−2.69 ± 0.15	−0.20 ± 0.13
Soil pit L6	200	L6-200-C	35.0	17.0	27.8	0.54	0.15	0.01	0.16	0.03	2.02	17.9	363	2.27	6.74	−2.37 ± 0.09	−0.12 ± 0.08
Vegetation																	
Above A4	–	A4-V	–	–	1.0	–	–	–	–	–	–	–	–	–	–	−1.90 ± 0.11	–
Above L6	–	L6-V	–	–	23.7	–	–	–	–	–	–	–	–	–	–	−1.78 ± 0.19	–
Bedload																	
LS01 (bulk)	–	LS01-B	22.5	9.7	28.4	0.68	0.63	1.72	0.81	0.12	1.49	15.3	302	–	–	−1.44 ± 0.09	–
LS01 (clay)	–	LS01-C	–	–	–	–	–	–	–	–	–	–	–	–	–	−2.52 ± 0.13	–
LS02 (bulk)	–	LS02-B	23.1	9.9	36.6	1.28	1.08	2.98	1.44	0.08	1.42	15.2	296	–	–	−1.06 ± 0.07	–
Suspended load																	
LS01	–	LS01-S	27.8	12.5	29.6	0.28	0.41	0.52	0.33	0.07	1.63	19.9	404	–	–	−1.91 ± 0.17	–
LS02	–	LS02-S	27.6	15.4	33.6	1.06	1.01	2.16	1.00	0.08	1.61	21.4	57	–	–	−1.34 ± 0.17	–
LS04	–	LS04-S	28.4	17.5	3.7	0.32	0.20	0.54	0.23	0.19	1.61	21.2	137	–	–	−2.37 ± 0.12	–
LS15	–	LS15-S	33.0	15.1	12.7	0.05	0.18	0.10	0.15	0.06	2.11	30.6	648	–	–	−2.59 ± 0.14	–

Note. No measurements were made where values are not given. The uncertainty is ±10% for K_2O and SiO_2 and ±3% for other all other elements.

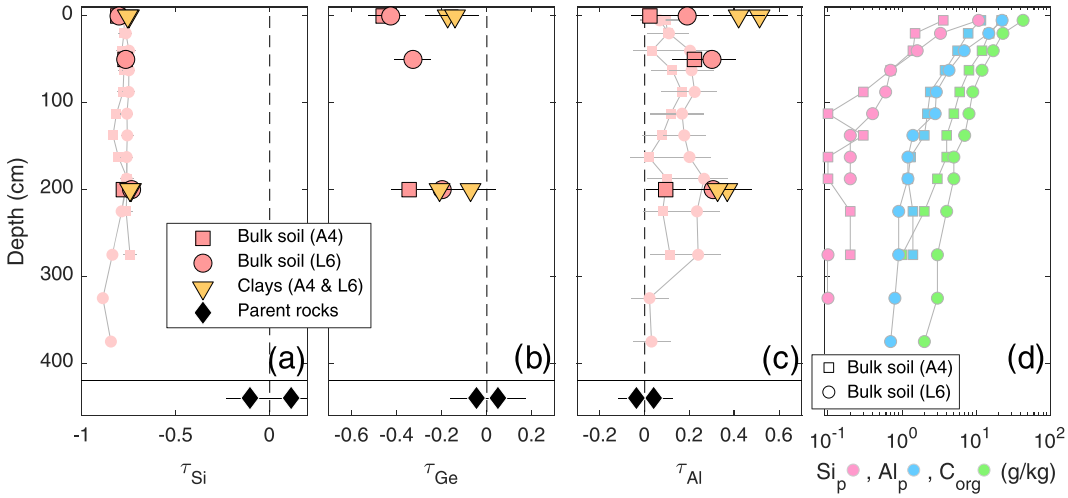

Figure 2. Changes in the chemical depletion ($\tau < 0$) or enrichment ($\tau > 0$) of (a) Si, (b) Ge, and (c) Al with depth, in bulk soils and separated clays. A4 is "old alluvial" soil developed on a river terrace, and L6 is "residual" soil developed on lava flows, both with similar andesitic parent material. The small symbols show values calculated using bulk soil data from the same soil pits previously published by Kleber et al. (2007). The concentrations of organic carbon, as well as pyrophosphate-extractable Si and Al determined by Kleber et al. (2007) are shown in (d). Pyrophosphate extraction targets organometallic complexes and, to a lesser degree, amorphous oxide phases (Parfitt & Childs, 1988; Wagai et al., 2013) and thus highlights the influence of vegetation litterfall to the distribution of Al and Si in the surface soil horizons.

groundwater from local wells are dilute and similar to rainwater with regard to major cation and anion concentrations, with the exception of slightly higher Ca and Mg (10–80 μmol/L in most cases) and significantly higher Si and Ge (50–140 μmol/L and 90–140 pmol/L, respectively). In contrast, local La Selva streams range from very dilute and similar to local groundwaters (e.g., Taconazo stream) to very concentrated, with Si and Na up to 1,300 μmol/L, Mg up to 1,100 μmol/L, Ca up to 600 μmol/L, and Cl up to 700 μmol/L (e.g., El Salto catchment). The concentrated streams are similar in composition to solute-rich IBGW, represented by a sample of Guacimo Spring (CR05) collected ~1 km south of the La Selva Biological Station (Figure 1).

3.3. Ge and Si Element and Isotope Distribution

The Ge and Si isotope composition and the Ge/Si ratios of the various samples are summarized in Figure 3 and Tables 1 and 2. The parent rock exhibits Ge/Si of 2.2 ± 0.1 μmol/mol, typical of volcanic rocks, whereas bulk soils show strongly elevated Ge/Si ratios of 6–6.5 μmol/mol, typically associated with secondary minerals such as kaolinite and Fe oxides (Kurtz et al., 2002; Lugolobi et al., 2010; Mortlock & Froelich, 1987). The separated clays are further enriched in Ge/Si, reaching values of 6.7–7.8 μmol/mol, consistent with higher degree of Ge retention relative to Si during chemical weathering (see section 4.3.2). In contrast, all fluids exhibit lower Ge/Si ratios than the rocks, with a local groundwater range of 1.4–2.0 μmol/mol, IBGW at 0.3 μmol/mol, and La Selva streams ranging widely between these extremes (0.4–1.3 μmol/mol).

Isotopically, all analyzed materials are significantly fractionated relative to the parent rock. The bulk soils are strongly depleted in heavy Si isotopes ($\delta^{30}Si_{soil} = -1.7$ to -2.5‰) and the separated clays are depleted further still ($\delta^{30}Si_{clay} = -2.4$ to -2.7‰), relative to the parent rock ($\delta^{30}Si_{rock} = -0.1$‰). Two different understory palm samples that exhibit very different degrees of Si content (SiO_2 weight fraction of 1.0% and 24%; Table 1) are isotopically light and indistinguishable from each other ($\delta^{30}Si_{veg} = -1.8$ to -1.9‰). La Selva groundwater and pore water composition is isotopically heavier than the bulk soils but in most cases still lighter than the parent rock ($\delta^{30}Si_{pw} = -1.3$ to 0.2‰; Figure 3c). Interbasin groundwater ($\delta^{30}Si_{IBGW} = 1.0 \pm 0.2$‰) is isotopically heavier than the parent rock, while La Selva streams span a wide range of values from 0.2 to 1.2‰, correlating with major solute concentrations and Ge/Si ratios (see discussion below).

Global Biogeochemical Cycles

10.1029/2019GB006522

Table 2
Chemical Composition of Fluids Sampled at La Selva Biological Station

Sample	Details	ID	Temp. (°C)	pH	Cond. (µS)	Alk. (meq/L)	Si (µM)	Na (µM)	Mg (µM)	K (µM)	Ca (µM)	Cl (µM)	SO_4 (µM)	Al (nM)	Fe (nM)	Ge (pM)	Ge/Si (µmol/mol)	δ^{30}Si ± 2σ (‰)	δ74Ge ± 2σ (‰)
Rainwater		LS16	–	–	–	–	4	60	8	4	5	60	13.4	399	194	9	2.3	–	–
Streams and groundwater seeps																			
Taconazo	At weir	LS01	25.1	5.6	9	0.06	120	60	12	9	14	53	6.5	644	689	107	0.89	0.29 ± 0.13	2.58 ± 0.12
Arboleda	At weir	LS02	24.9	6.5	276	2.49	1070	768	533	125	400	355	46.1	431	649	423	0.40	1.03 ± 0.12	3.25 ± 0.12
El Salto	East trib.	LS04	24.4	6.5	16	0.15	232	93	22	–	29	51	5.8	409	449	88	0.38	0.46 ± 0.18	3.05 ± 0.12
El Salto	GW seep	LS05	25.3	6.7	424	4.07	1260	1250	877	173	529	619	76.8	843	164	498	0.39	1.27 ± 0.21	–
El Salto	Tributary	LS06	25.8	6.6	233	4.68	1290	1340	1080	236	624	678	86.3	265	225	505	0.39	1.12 ± 0.14	3.61 ± 0.12
El Salto	Main stem	LS07	25.2	7.1	157	1.22	550	464	327	74	209	237	28.5	643	832	231	0.42	1.03 ± 0.10	3.35 ± 0.12
El Sura	Main stem	LS08	25.5	6.6	10	0.09	167	72	18	16	19	46	5.2	274	380	90	0.54	0.57 ± 0.15	–
Piper	Main stem	LS09	25.4	6.0	13	0.12	151	67	24	9	28	50	5.7	266	478	89	0.59	0.70 ± 0.14	–
Quebrada Esquina		LS10	25.1	6.8	21	0.20	284	96	31	31	42	52	5.1	1190	511	104	0.37	0.92 ± 0.26	3.02 ± 0.12
El Saltito	GW seep	LS11	25.1	6.0	6	0.04	196	64	8	16	8	49	5.2	475	502	131	0.67	0.67 ± 0.27	2.63 ± 0.12
Taconazo	At weir	LS12	–	–	10	0.06	143	60	13	11	15	50	5.2	319	299	103	0.72	0.64 ± 0.20	–
Arboleda	At weir	LS13	–	–	142	3.10	1140	839	583	139	439	379	49.0	638	569	455	0.40	1.23 ± 0.15	–
Taconazo	Upstream	LS14	25.7	5.4	10	0.02	77	60	13	15	12	59	9.5	907	549	97	1.26	0.38 ± 0.15	2.39 ± 0.12
Arboleda	Upstream	LS15	26.2	5.4	14	0.02	88	65	16	22	12	62	14.2	781	278	101	1.14	0.19 ± 0.09	2.60 ± 0.12
El Saltito	Main stem	LS17	–	–	117	0.94	423	307	209	45	144	167	21.5	661	739	188	0.44	1.03 ± 0.13	–
Regional rivers																			
Rio Sarapiqui	At Puerto Viejo	CR01	27.2	7.2	50	0.43	279	–	–	–	–	58	34.2	1680	847	136	0.49	1.32 ± 0.14	–
Rio Sarapiqui	At Sardinal	CR02	25.8	7.1	27	0.39	295	–	–	–	–	114	180.0	565	168	120	0.41	1.34 ± 0.26	–
Rio Sarapiqui	At San Miguel	CR03	22	8.0	117	0.87	684	–	–	–	–	94	158.4	2050	544	177	0.26	1.52 ± 0.21	–
Interbasin groundwater																			
Guacimo	Spring (“old”)	CR05	25.4	6.4	590	–	1300	1340	1490	–	757	733	125.8	308	366	405	0.31	1.02 ± 0.24	4.02 ± 0.12
Local groundwater (wells)																			
Farm	–	LS03	25.1	5.2	20	0.04	51	70	8	–	23	60	18.2	324	472	97	1.91	0.06 ± 0.13	2.24 ± 0.12
Taconazo	–	LS18	–	–	–	–	74	56	11	3	13	53	9.5	1920	119	99	1.35	0.17 ± 0.14	–
Saltito	60 cm	LS19	–	–	–	–	53	71	22	7	25	49	7.5	5920	735	92	1.75	0.21 ± 0.18	–
Salto	60 cm	LS20	–	–	–	–	69	60	16	6	16	53	7.6	2070	587	135	1.97	−0.67 ± 0.07	–
Salto	100 cm	LS21	–	–	–	–	87	84	17	–	17	52	8.5	17600	3980	–	–	−0.40 ± 0.26	–
Soil pore water																			
Soil pit A4	0 cm	A4-0-W	–	–	–	–	72	122	62	–	175	63	44.8	12040	–	–	–	−1.25 ± 0.08	–
Soil pit A4	25 cm	A4-25-W	–	–	–	–	52	87	18	–	59	66	22.5	294	–	–	–	−1.02 ± 0.10	–
Soil pit A4	50 cm	A4-50-W	–	–	–	–	53	101	22	–	62	56	26.3	295	–	–	–	−1.21 ± 0.08	–
Soil pit A4	200 cm	A4-200-W	–	–	–	–	45	67	23	–	52	73	12.6	915	–	–	–	−0.96 ± 0.09	–
Soil pit L6	0 cm	L6-0-W	–	–	–	–	139	120	50	–	79	103	35.1	23900	–	–	–	−0.03 ± 0.11	–
Soil pit L6	50 cm	L6-50-W	–	–	–	–	43	81	13	–	32	69	17.5	331	–	–	–	−1.04 ± 0.08	–
Soil pit L6	200 cm	L6-200-W	–	–	–	–	33	54	10	–	36	40	18.8	61	–	–	–	0.02 ± 0.10	–

Note. No measurements were made where values are not given. The analytical uncertainty for all solutes is within 10% (2 SD).

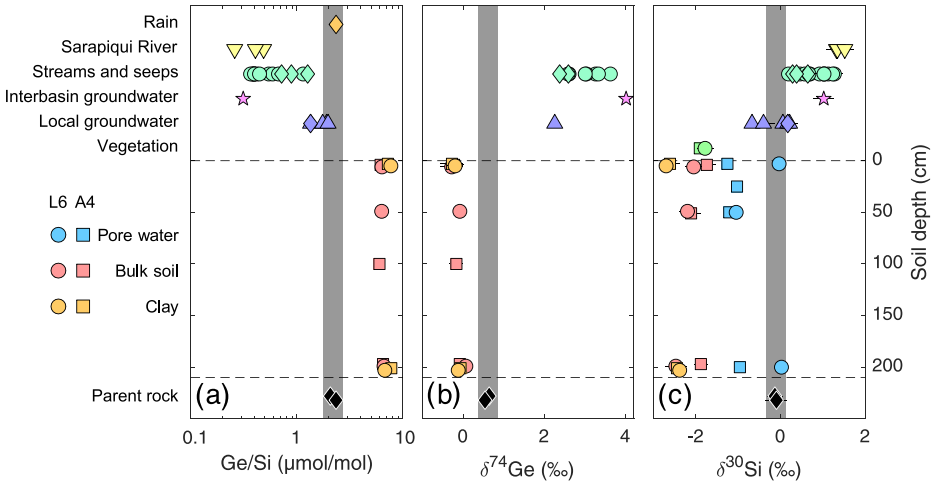

Figure 3. Silicon and germanium isotope and Ge/Si ratios of all samples in this study. The depth scale (y axis) on the right applies to the bulk soil, separated clay, and pore water samples only. Taconazo watershed stream and well samples (thought to represent the local weathering end-member) are shown as light green and purple diamonds, respectively. Where not visible, 2σ error bars are smaller than the symbols.

Similarly to δ^{30}Si, light Ge isotopes are enriched in soils and clays (δ^{74}Ge = -0.1 to -0.3‰) relative to parent rock ($\delta^{74}Ge_{rock}$ = 0.6‰), whereas local groundwater (2.2‰), IBGW (4.0‰), and local streams (2.4–3.6‰) are all isotopically heavy relative to the parent rock (Figure 3b). Ge/Si, δ^{30}Si, and δ^{74}Ge composition of bulk soils, separated clays, and soil pore waters are all relatively constant with depth within uncertainty (Figure 3). A crossplot of δ^{30}Si versus Ge/Si and versus δ^{74}Ge for all samples measured in this study is given in Figure S7.

4. Discussion

The results of this study are consistent with recent findings of close coupling between Ge/Si, δ^{30}Si, and δ^{74}Ge in global rivers (Baronas et al., 2018). All three proxies primarily reflect fractionation during weathering, with secondary phases enriched in light isotopes and Ge relative to Si (Table 1), leaving fluids with isotopically heavier and low Ge/Si signatures (Table 2). In addition, vegetation uptake affects dissolved Ge/Si and δ^{30}Si signatures (e.g., Cornelis et al., 2010), while it appears to have a smaller (but poorly quantified) effect on δ^{74}Ge (Baronas et al., 2018). Importantly, our study site at La Selva represents an advanced chemical weathering environment, with both the bulk soils and the local soil- and stream waters showing some of the lightest Ge and Si isotope compositions measured to date.

Below, we discuss (1) the role of mixing between local lowland fluids and IBGW in controlling the chemical and isotopic signatures of streams in this study area; (2) Ge and Si isotope fractionation during the weathering of volcanic lavas by IBGW, informed by a kinetic reactive transport model; (3) the uptake of Si and Ge by vegetation and clay neoformation, quantified using a simple mass balance model, and the link between these processes; and (4) the global relationship between the weathering intensity (chemical depletion) recorded in secondary weathering products (bulk soils and clays) and their Ge/Si, δ^{30}Si, and δ^{74}Ge signatures.

4.1. Stream Chemistry Controlled by Mixing of Local Fluids and Volcanic IBGW

The first-order control on the composition of La Selva streams is the mixing of dilute lowland surface water with solute-rich volcanic IBGW sourced from higher elevation on the slopes of Barva Volcano (e.g., Genereux & Jordan, 2006; Genereux et al., 2009; Pringle et al., 1990), some tens of kilometers south of the study site (Figure 1). Our most representative sample of IBGW is from Guacimo Spring (CR05), exhibiting Si, Na, and Cl concentrations of 1.30, 1.34, and 0.73 mmol/L, respectively. Previous work showed the composition of this spring to be stable over several years of varying hydrological conditions (Na = 1.92 ± 0.44 mmol/L, Cl = 0.90 ± 0.10 mmol/L, 2 SD, n = 56; Genereux et al., 2002). Within the La Selva research

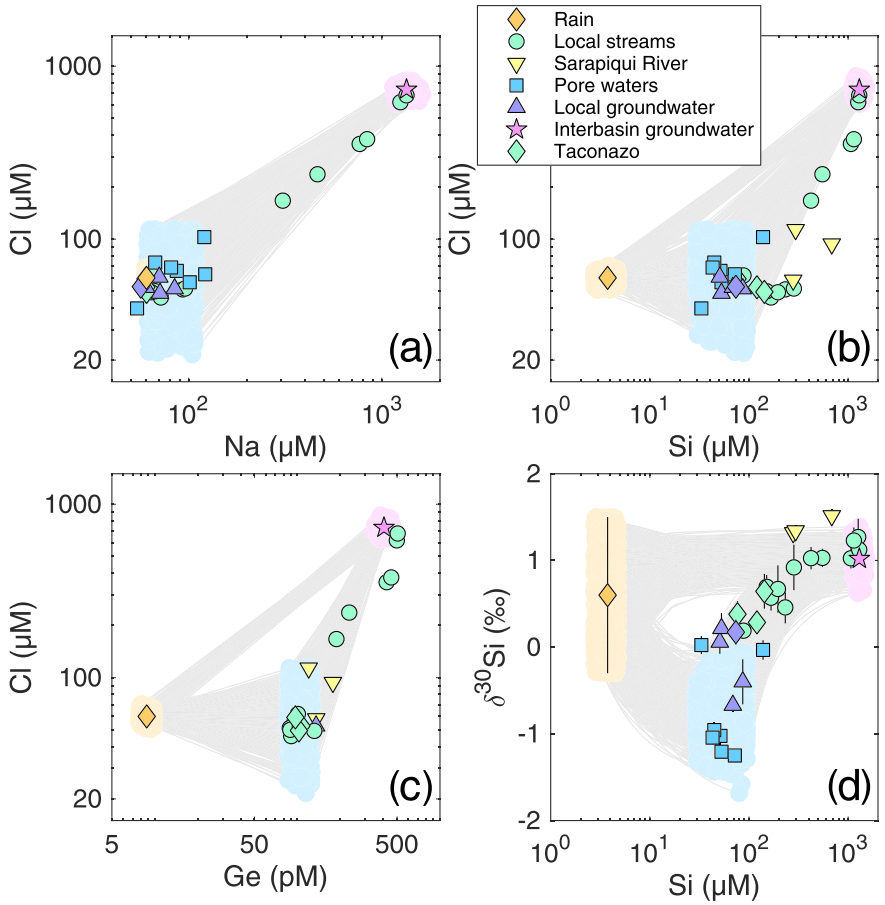

Figure 4. The range of chemical and δ^{30}Si compositions in La Selva streams and other water samples. In each panel, the gray area shows the mixing space between rainwater, lowland weathering fluids (all pore waters and well samples), and interbasin groundwater (Guacimo Spring sample CR05, pink star). The mixing space is calculated from 1,000 Monte Carlo simulations, randomly sampling each end-member (shaded area around the measured sample compositions of the three end-members) from a range of values defined either by analytical uncertainty (for groundwater and rain water) or 2 SD of all pore water and well samples (for the local lowlands end-member). Rainwater composition is included to highlight the fact that soil pore waters inherit only negligible Si and Ge from rain. For rainwater, δ^{30}Si was not measured; therefore, for visualization purposes, a range of values anywhere between –0.3 and 1.5‰ was assigned, encompassing most measured silicate rock and seawater values (Frings et al., 2016).

station, IBGW input affects each stream to a different degree and its influence can also vary within a watershed. This heterogeneity is well exemplified by comparing two streams where samples were taken at different points along each stream (Table 2). In the Taconazo watershed, the upstream chemistry (LS14) is very similar to the outlet (LS01/LS12), consistent with negligible contribution from IBGW, whereas in the Arboleda watershed, the upstream fluid (LS15) is very similar to the Taconazo, but the stream water sampled at the outlet (LS02) is highly enriched in solutes and closely resembles the chemistry of pure IBGW end-member, exemplifying the localized IBGW discharge in the lowlands of the La Selva Biological Station.

The two end-member mixing between lowland fluids and IBGW is clearly visible in Na-Cl space (Figure 4a). In Ge-Cl and Si-Cl mixing space (Figures 4b and 4c), it is apparent that not all dissolved Ge and Si are derived from IBGW because local streams plot on a mixing line between IBGW and local soil waters (rather than rainwater). These trends indicate that weathering of the local, lowland soils also supplies Ge and Si to the streams.

Interestingly, some La Selva streams fall outside of the mixing space between local soil waters and IBGW, indicating another source of Si (and to lesser extent, Ge). This source appears to have a low Ge/Si ratio

Table 3
Summary of Calculated Parameters for Weathering of Volcanic Rocks Via Interbasin Groundwater (section 4.2) and La Selva Lowlands Soils (section 4.3.1)

Parameter	Calculated value	
	Interbasin groundwater	Lowland soils
$f_{diss}Si$	~0.25	0.005 ± 0.004
$f_{sec}Si$	~0.75	0.61 ± 0.14
$f_{bio}Si$	–	0.39 ± 0.14
$f_{diss}Ge$	~0.03	0.002 ± 0.002
$f_{sec}Ge$	~0.97	0.91 ± 0.09
$f_{bio}Ge$	–	0.09 ± 0.09
$\Delta^{30}Si_{sec\text{-}diss}$	−1.2 ± 0.2‰	−1.7 ± 0.5‰
$\Delta^{30}Si_{bio\text{-}diss}$	–	−1.0 ± 0.5‰
$\Delta^{74}Ge_{sec\text{-}diss}$	−3.0 ± 0.5‰	−2.3 ± 0.2‰
$\Delta^{74}Ge_{bio\text{-}diss}$	–	–
$\alpha_{sec}^{Ge/Si}$	10 ± 1	3.4 ± 1.0
$\alpha_{bio}^{Ge/Si}$	–	0.62 ± 0.28

Note. Uncertainties given as 1 SD.

and a relatively low Cl content, compared to IBGW, and seems to have a higher contribution in the larger Sarapiqui River (Figure 4b). We speculate that this source of Si might be from weathering closer to the regolith-bedrock interface, some tens of meters deeper than our 2 m deep soil pits. Ultimately, all local fluids likely lie on a continuous spectrum of composition between (1) weathering of the surficial soils and (2) weathering of primary minerals at the local regolith-bedrock interface encountered much deeper. The latter process, however, must not be confused with the volcanic rock-water interaction that yields the IBGW signature, as discussed in more detail below (section 4.2). Similar contribution from deep fluids reflecting weathering at the regolith-bedrock interface has been observed in tropical streams of Puerto Rico, both in Ge/Si signatures in a granitic catchment (Kurtz et al., 2011) and Mg isotopic signatures in an andesitic catchment (Chapela Lara et al., 2017). Importantly, the Si isotope composition of La Selva streams lies almost exclusively on the two end-member mixing trend between shallow soil waters and IBGW (Figure 4d). This suggests that *local* deep fluids have limited influence on δ^{30}Si signatures of La Selva streams, relative to the first-order control by mixing of soil waters with IBGW.

The evolution of Ge and Si signatures in La Selva weathering fluids can therefore be summarized as follows. Dilute rainwater percolates shallow soils, where weathering (and potentially organic litter decomposition) adds a relatively small *net* amount of dissolved Ge and Si. Some portion of these fluids percolate to the regolith interface where they may gain additional Si. Finally, depending on particular catchment and location, some of these local fluids are mixed with varying proportions of IBGW, resulting in the wide range of sampled compositions. In sections 4.2–4.3, we focus on understanding the processes that control the compositions of the two contrasting end-member fluids: the volcanic IBGW and the shallow lowland soil water.

4.2. Modeling Ge and Si Isotope Fractionation in IBGW

The interbasin groundwater (IBGW) is thought to percolate through extensive layered volcanic tuff aquitards as it descends into the lowlands where the La Selva study area is located (Genereux et al., 2009). The δ^{30}Si signature of IBGW is similar to that observed in other weathering environments where secondary clay precipitation during silicate weathering results in isotopically heavy river or ground water (e.g., Frings et al., 2016; Georg et al., 2006a; Hughes et al., 2013; Ziegler et al., 2005). It must be noted that isotopically light groundwater signatures have also been documented elsewhere, likely reflecting the dissolution of secondary clays in sedimentary rock-hosted aquifers (Georg, West, et al., 2009; Georg, Zhu, et al., 2009; Pogge von Strandmann et al., 2014). However, we expect that the groundwaters from Volcan Barva reflect weathering of the primary andesitic material accompanied by secondary mineral formation, which is consistent with the low Ge/Si ratio of 0.3 μmol/mol in IBGW. While there are no previous published groundwater δ^{74}Ge data available for comparison, the isotopically heavy signature of IBGW is consistent with the broad negative correlation between Ge/Si and δ^{74}Ge observed by Baronas et al. (2018) in global rivers.

Based on ^{14}C dating of dissolved inorganic carbon, the transit time of IBGW is longer than 2,000 years, although this estimate might be affected by partial isotopic exchange with magmatic CO_2 (Genereux et al., 2009). Nevertheless, such a long fluid transit timescale suggests that IBGW fluids may have reached a chemical and isotopic equilibrium with the reactive volcanic rock and the precipitating secondary phases by the time they discharge at La Selva, which is also consistent with the interannually stable solute concentrations of IBGW (Genereux & Jordan, 2006). In order to test whether our isotopic data are consistent with equilibrium weathering conditions, we adapted a reactive transport model initially developed to investigate U-Th series isotopes in groundwater by Tricca et al. (2000) and Porcelli (2008) and later applied to Li isotopes by Pogge von Strandmann et al. (2014). The details of the model are described and the derivation of key equations is given in Text S2.

To obtain a conservative estimate of fluid equilibration timescale, we used a mineral dissolution rate constant (10^{-16} mol m^{-2} s^{-1}) that is at the lower end of field-derived plagioclase weathering rates (Brantley

et al., 2008). Including a simple representation of thermodynamic control on rates based on transition state theory (e.g., Schott et al., 2009), we calculated that IBGW fluids should reach steady state (with regard to both Si and Ge concentrations and their isotopic compositions) within less than 600 years, or about 2 km of subsurface flow (see Figure S5), whereas the minimum distance between the IBGW recharge area and La Selva is estimated to be ~9 km, ignoring tortuosity of the subsurface flowpaths (Genereux et al., 2009). At steady state, the isotopic difference between the IBGW fluid and the volcanic rock with which it had equilibrated should directly reflect the fractionation factor associated with Si and Ge removal from solution into secondary phases during groundwater transit (e.g., $\Delta^{30}Si_{sec-diss} = \delta^{30}Si_{rock} - \delta^{30}Si_{IBGW}$; see Equation S8). Using the mean isotopic composition of the IBGW-dominated fluids (i.e., samples LS02, LS05, LS06, LS13, and CR05; Table 2) yields the following isotope fractionation factors: $\Delta^{30}Si_{sec-diss} = -1.2 \pm 0.3‰$ and $\Delta^{74}Ge_{sec-diss} = -3.0 \pm 0.9‰$ (Table 3). This model does not make an implicit assumption on the removal mechanism (e.g., coprecipitation vs. net adsorption), with the only implication being that it is a first-order kinetic process.

Because the reactive transport model tracks the amount of Si and Ge removed from solution, it can be used to calculate the fraction of total dissolved Si and Ge remaining in the final IBGW fluid ($f_{diss}Si = 0.25$, $f_{diss}Ge = 0.03$; Table 3) and the accumulated secondary phase composition ($\delta^{30}Si_{sec} = -0.49‰$, $\delta^{74}Ge_{sec} = 0.49‰$; Figure S5). Applying the often-used steady state equilibrium model ($\Delta_{sec-diss} = \delta_{sec} - \delta_{diss}$; Bouchez et al., 2013; Johnson et al., 2004) to these values yields fractionation factors $\Delta^{30}Si_{sec-diss} = -1.6‰$ and $\Delta^{74}Ge_{sec-diss} = -3.2‰$, respectively. The agreement between these values and the measured difference between initial rock composition and the final IBGW fluid ($\Delta^{30}Si_{sec-diss}$ and $\Delta^{74}Ge_{sec-diss}$ values given above) provides additional evidence that the kinetic reaction rates and other parameters used in the model (Table S4) are not unreasonable. Both Si and Ge isotope fractionation factors calculated here are within the range of values determined previously for a number of global rivers (Baronas et al., 2018), as well as experimental results on adsorption or coprecipitation with a range of secondary phases in the case of Si (Delstanche et al., 2009; Frings et al., 2016; Oelze et al., 2014, 2015) and with Fe oxides in the case of Ge (Pokrovsky et al., 2014).

4.3. Lowland Critical Zone Processes

The small watersheds in the La Selva lowlands represent a weathering regime that is very different from the IBGW system. Due to the warm and humid tropical climate combined with low denudation rates, the soils of La Selva are entirely depleted of primary minerals (with the exception of some unreactive quartz) and major cations and therefore represent an extreme example of an erosion-limited weathering regime (see section 3.1). Progressive weathering has resulted in the formation of thick (up to 20 m) Oxisols that are enriched in light Si and Ge isotopes (Figure 3). At present, the upper soils are being gradually desilicified and soil clays (dominantly kaolinite) are in the process of being converted into neoformed poorly crystalline Al-Si-Fe phases (Kleber et al., 2007), which results in further fractionation of $\delta^{30}Si$, $\delta^{74}Ge$, and Ge/Si. In this section, we explore how these processes generate distinct geochemical tracer signatures in the lowland soil waters and streams unaffected by IBGW inputs (Figure 3). Using a simple isotope mass balance model, we obtain a snapshot of the current, "short-term" Ge and Si cycle on a soil profile scale in a setting with very high chemical weathering intensity.

4.3.1. Partitioning and Fractionation of Si and Ge Between Different Compartments

On a soil profile scale, water inputs are spatially distributed and flowpaths are short, on the scale of meters, making a single-flowpath reactive transport model such as that applied to IBGW (section 4.2) unsuitable for modeling soil-scale weathering. Instead, we employ a simple mass balance (a.k.a., "mixed open system") model, recently developed for the coupled Ge/Si isotope system and applied on a catchment scale by Baronas et al. (2018). We use this model to understand the fate of Si and Ge released from the soils during chemical weathering, partitioning these elements between export in the dissolved phase (represented by pore water), uptake by neoforming phases (which we refer to as "clays" from here on for simplicity, emphasizing the size-based separation methodology, while acknowledging that this material contains both aluminosilicate and oxide phases) and uptake by the abundant tropical vegetation. This framework is impartial to the exact isotope fractionation mechanism (kinetic or equilibrium) and assumes that the system (soil profile) as a whole is at a (quasi) steady state, that is, any change in the chemical composition of the different solid compartments is slow relative to the timescale at which the pore water composition attains its signature

(Bouchez et al., 2013). In other words, the isotopic composition of the mineral and vegetation compartments is deemed stable over fluid transit timescales. This quasi-steady state assumption, however, does not imply a chemical or isotopic equilibrium between the different phases, nor that the landscape is in steady state over longer timescales (i.e., the model does not require stable weathering fronts).

The model is described in detail in Baronas et al. (2018) and only slightly modified here to make better use of the clay and vegetation data collected in this study (see detailed description in Text S3). Briefly, we use the Si/Na and Ge/Na ratios in the dissolving material (represented by the sampled bulk soils) and the fluids (represented by the sampled soil pore waters) to determine the fraction of each element remaining in solution (f^{Si}_{diss} and f^{Ge}_{diss}), followed by using δ^{30}Si mass balance to determine the exact partitioning of Si uptake between clays (f^{Si}_{sec}) and vegetation (f^{Si}_{bio}) and Ge/Si mass balance to determine f^{Ge}_{sec} and f^{Ge}_{bio}. We use the Monte Carlo method to estimate the uncertainty of the calculated parameters. At steady state, the isotopic fractionation factors are equal to our measured difference in isotopic composition of the three phases, namely,

$$\Delta^{30}Si_{sec-diss} = \delta^{30}Si_{clay} - \delta^{30}Si_{porewater} \quad (1)$$

$$\Delta^{30}Si_{bio-diss} = \delta^{30}Si_{veg} - \delta^{30}Si_{porewater} \quad (2)$$

$$\Delta^{74}Ge_{sec-diss} = \delta^{74}Ge_{clay} - \delta^{74}Ge_{porewater} \quad (3)$$

yielding values of $\Delta^{30}Si_{sec-diss} = -1.7 \pm 0.5‰$, $\Delta^{30}Si_{bio-diss} = -1.0 \pm 0.5‰$, and $\Delta^{74}Ge_{sec-diss} = -2.3 \pm 0.2‰$ (median $\pm$ 1 SD; Table 3).

Mineralogical studies of La Selva soils indicate the ongoing conversion of kaolinite into mostly amorphous Al-Si oxides (some combination of allophane, halloysite, and/or gibbsite) (Kautz & Ryan, 2003; Kleber et al., 2007; Sollins et al., 1994), as discussed in more detail below. Multiple recent experimental studies have shown that $\Delta^{30}Si_{sec-diss}$ fractionation factors associated with amorphous silica and Si-Al oxide precipitation can range from −5 to 0‰, with higher fractionation induced by far-from-equilibrium conditions (Fernandez et al., 2019; Oelze et al., 2014, 2015; Roerdink et al., 2015). Similarly, $\Delta^{74}Ge_{sec-diss}$ during reversible Ge adsorption onto Fe (oxy)hydroxides was smaller (–1.7 ‰) than during irreversible coprecipitation (down to –4.4‰), likely representing dominantly close to equilibrium and far-from-equilibrium conditions, respectively (Pokrovsky et al., 2014). Our results therefore suggest incomplete Si (and possibly Ge) isotope equilibration between pore waters and neoforming solids in the soils studied here.

In addition to isotopic fractionation, our mass balance model yields estimates of Ge/Si fractionation associated with clay and vegetation uptake of the two elements. We calculate fractionation factor $\alpha^{Ge/Si}_{sec} = 3.4 \pm 1.0$ (defined as $(Ge/Si)_{sec}/(Ge/Si)_{diss}$; Baronas et al., 2018) or $K_{sec} = 1.5 \pm 0.3$ (defined as $(Ge/Si)_{sec}/(Ge/Si)_{ini}$, equivalent to K_w in Froelich et al., 1992, where $(Ge/Si)_{ini}$ is the composition of the dissolving minerals, in this case represented by bulk soils). Similarly, the biological fractionation factor is $\alpha^{Ge/Si}_{bio} = 0.62 \pm 0.28$ (defined as $(Ge/Si)_{veg}/(Ge/Si)_{diss}$). Calculated independently of any Ge/Si measurements in vegetation, this value is nevertheless in line with previous studies, which had shown a similar degree of discrimination against Ge by plants (Blecker et al., 2007; Cornelis et al., 2010; Delvigne et al., 2009; Meek et al., 2016).

Although the Ge/Si composition of secondary phases precipitating during IBGW flow cannot be measured directly, it can be calculated using the reactive transport model (Text S2), yielding 3.9–4.1 μmol/mol and thus an $\alpha^{Ge/Si}_{sec}$ value of 10 ± 1. The $\alpha^{Ge/Si}_{sec}$ values determined in both the IBGW and lowland soil environments (Table 3) are in agreement with the global range of values (2–22) reported by Baronas et al. (2018) using data from catchments of different sizes from around the world. The higher value calculated for IBGW may indicate the dominance of different secondary phases or a difference in the equilibrium versus kinetic fractionation character between the two (lowland soil vs. volcanic aquifer) weathering environments. Notably, the isotopic fractionation factors ($\Delta^{30}Si_{sec-diss}$ and $\Delta^{74}Ge_{sec-diss}$) are less distinct and indeed indistinguishable between the two weathering environments given the calculated 2 SD uncertainties (Table 3).

Finally, the main purpose of our model is to calculate how the release of Si and Ge from soils via weathering is partitioned between the three phases, namely, neoformed clays, vegetation (primarily phytoliths), and solution. The results (Table 3) show that in the upper 2 m of soil, the majority of Si is taken up by

neoforming clays (f_{sec}Si = 61 ± 14%), with a significant portion taken up by vegetation (f_{bio}Si = 39 ± 14%) and only a small fraction remaining as dissolved silica in the pore water (f_{diss}Si = 0.5 ± 0.4%). In contrast, Ge is almost exclusively removed by neoforming clays (f_{sec}Ge = 91 ± 9%), with only a small portion taken up by vegetation (f_{bio}Ge = 9 ± 9%) and an even smaller fraction remaining in solution (f_{diss}Ge = 0.2 ± 0.2%).

4.3.2. The Ecosystem Effects on the Soil Si Cycle and Weathering

It is important to preface the following discussion by noting that the partitioning of Ge and Si between neoforming clays and ecosystem uptake is strongly dependent on the measured δ^{30}Si composition of just two vegetation samples, which may not be representative of the average local vegetation composition. However, (1) the sampled plants were selected because they were visually abundant in the studied area; (2) their Si wt% content spans more than an order of magnitude (Table 1), bracketing most types of plants sampled to date (Hodson et al., 2005; Song et al., 2016); (3) the modeling results described above depend only on $\delta^{30}Si_{veg}$ and are independent of vegetation Si wt% content; (4) the measured $\delta^{30}Si_{veg}$ compositions of the two samples were very similar to each other (Table 1); and (5) the calculated vegetation fractionation factor ($\Delta^{30}Si_{bio-diss} = -1.0 \pm 0.5‰$) is consistent with previous studies (Frings et al., 2016). Even though $\delta^{30}Si_{veg}$ is the least sampled ($n = 2$) Si reservoir in our soil mass balance model, notably, the uncertainty range of $\Delta^{30}Si_{bio-diss}$ determined here brackets the majority of previously reported values globally (Frings et al., 2016) and therefore accounts for the full effect of the $\delta^{30}Si_{veg}$ uncertainty on the model results.

From a long-term mass balance perspective, the ecosystem impact on the catchment-wide Si cycle depends on the efficiency of phytolith Si export out of the catchment. Recently, Uhlig et al. (2017) and Schuessler et al. (2018) quantified the dissolved export efficiency of Si (equivalent to f_{diss}Si/f_{bio}Si ratio) in an erosion-dominated montane catchment and a tropical transport-limited catchment, respectively. In the tropical erosion-limited catchment, which shares many similarities to La Selva, only a negligible fraction of Si was exported as amorphous phytoliths, that is, f_{diss}Si >> f_{bio}Si, whereas about half of bioavailable Si was exported in the form of phytoliths in the erosionally dominated system (f_{diss}Si ≈ f_{bio}Si). The Si mass balance for these studies was established by comparing stream dissolved composition (present day f_{diss}Si) with long-term element loss through chemical weathering (regolith-averaged τ_{Si}), relative to initial parent rock.

In contrast, our δ^{30}Si-based mass balance model indicates that f_{bio}Si is ~70 times higher than f_{diss}Si in the La Selva lowland soils, indicating the almost complete uptake of bioavailable Si by local vegetation, despite extremely low rates of erosion. This discrepancy is likely explained by the difference in spatial and temporal scales considered here and in Schuessler et al. (2018). In the present study, we focus on the pedogenic perspective, using the present-day δ^{30}Si mass balance of the upper 2 m of soil only. In this case, pore water solutes are acquired via the weathering of secondary phases and the dissolution of phytoliths in the upper soil (as it is devoid of primary minerals), which are acting as the "parent" material instead of bedrock, only encountered some 10–20 m deeper. The Si and Ge partitioning investigated here is therefore driven by upper soil-scale dynamics, rather than the erosional regime of the whole catchment, such as that in Schuessler et al. (2018). The mass balance presented in section 4.3.1 may thus reflect localized and/or transient accumulation of amorphous Si (aSi) phases in standing vegetation and/or upper soils.

Given that the dominant plant rooting depth in the studied La Selva soils is around 1 m (Veldkamp et al., 2003), the high f_{bio}Si/f_{diss}Si ratio may reflect the localized uptake of Si by plants within the studied soil horizons. Several previous studies have postulated significant phytolith accumulation in tropical soils (e.g., Clarke, 2003; Meunier et al., 1999; Song et al., 2012), and especially efficient preservation within microaggregate particles (Li, de Tombeur, et al., 2020), which may allow a fraction of phytolith aSi to be efficiently preserved within the top 2 m soil and possibly deeper. The proportional dominance of plant-recycled Si in highly weathered soils was also recently directly demonstrated using rice growth experiments in the lab (Li, Cornelis, et al., 2020). Although any such enrichment is too small to be visible in τ_{Si} (Figure 2a), the fraction of amorphous or organocomplexed Si increases up to 1 wt% in surface soils, supporting potential accumulation of phytoliths (Figure 2d, see discussion below).

It is also possible that the model results reflect a nonsteady state system, that is, a perturbation over timescales longer than that required for the pore waters to obtain their signature. For example, Wood et al. (2006) have shown that nutrient concentrations in leaf litter can vary significantly over seasonal and interannual timescales, potentially driven by variations in rainfall. In addition, anthropogenic perturbation and

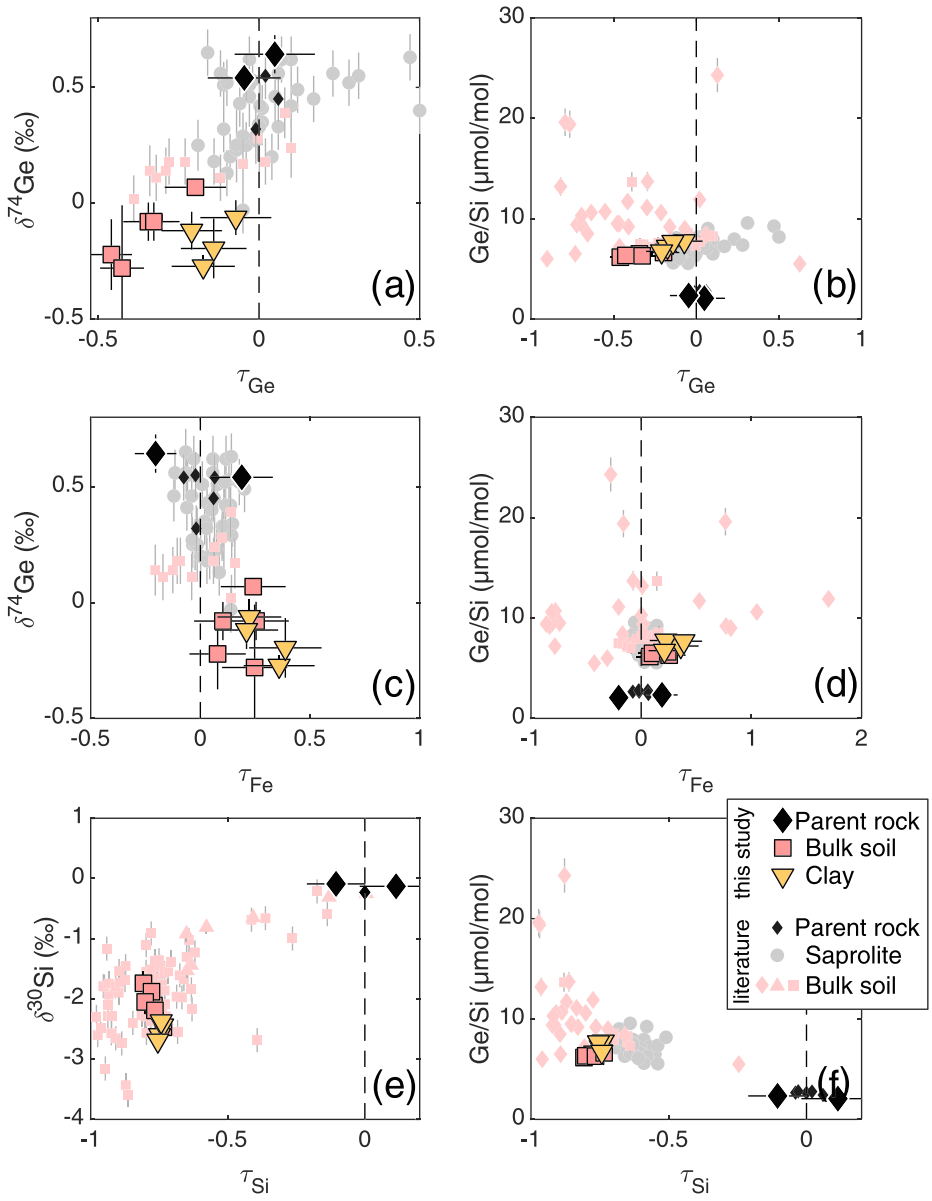

Figure 5. Relationships of δ^{74}Ge, δ^{30}Si, and Ge/Si versus fractional elemental loss ($\tau < 0$) or gain ($\tau > 0$) of Ge, Fe, and Si in volcanic soils (Equation S1). Small symbols are published values of Kurtz et al. (2002) (Ge/Si; diamonds) and Bern et al. (2010) (δ^{30}Si corrected for dust inputs; squares) for basaltic soils in Hawaii, Qi et al. (2019) for a basaltic weathering profile in Hainan island, China (δ^{74}Ge and Ge/Si; squares and circles), and Opfergelt et al. (2012) for an andesitic soil sequence in Guadeloupe island, French Indies (δ^{30}Si; triangles).

long-term climate change could also affect nutrient dynamics over centennial and millennial timescales, respectively. It is feasible that the local Si biogeochemical cycle is to some degree perturbed over any of these timescales, resulting in the significant net Si uptake by vegetation, as identified by our Si isotope mass balance model described above.

Despite the net Si uptake and the potential preservation or export of some aSi, the supply and remineralization of leaf litter appears to have important influence on the elemental cycling and chemical weathering reactions in the upper La Selva soils. The values of τK, τCa, and τMg all increase towards the surface, indicating a top-down supply of these nutrients via leaf litter (i.e., a biopump effect). The high degree of control that the La Selva forest vegetation exhibits on the cycling of limiting nutrients (excluding Si) has been

demonstrated previously (Wood et al., 2006). The persistence of rock-derived Sr, as evidenced using $^{87/86}$Sr signatures, also supports the efficient recycling of nutrients in this ecosystem (Porder et al., 2006).

The vegetation Si biopump also has important consequences for the ongoing chemical weathering of the upper soils. Extremely low erosion and depletion of primary minerals have been shown to typically result in congruent weathering of silicates, accompanied by the destabilization and dissolution, rather than formation, of amorphous Al-Si phases and clays like kaolinite (Gaillardet et al., 1995; Murnane & Stallard, 1990; Stallard & Edmond, 1983; Viers et al., 2000). Despite this, both previous clay mineralogical data (Kleber et al., 2007) and our mass balance model results (high f_{sec}Si and f_{sec}Ge values, Table 3) indicate efficient ongoing clay neoformation at La Selva. The higher Ge/Si of the clay fraction relative to the bulk soils (Table 1) is also consistent with the well-documented preferential incorporation of Ge in solid phases formed during chemical weathering, such as aluminosilicates and Fe oxyhydroxides (Kurtz et al., 2002; Lugolobi et al., 2010; Murnane & Stallard, 1990). Active neoformation of clays is also corroborated by the positive τAl values in the upper 3 m of soil, and especially so in the surface horizon clay fraction (Figure 2c), reflecting the formation of Al-rich secondary phases (supergene enrichment). External input of elements via dust deposition is thought to be low at La Selva (Porder et al., 2006) and is an unlikely source of extra Al. Localized supergene enrichment (τAl > 0) should typically be accompanied by a shallower leached (τAl < 0) horizon, which was not encountered in the La Selva soil pits. It is therefore possible that this horizon was eroded away relatively recently (e.g., due to anthropogenic disturbance) or that it is very thin and is not revealed at the current sampling resolution. Finally, the top-down supply of Al and Si available for clay neoformation is also illustrated by the large increase in organically complexed and amorphous Al and Si at the soil surface (Figure 2d), quantified using pyrophosphate extraction by Kleber et al. (2007). Taken together, all these observations add to the increasing pool of evidence that vegetation can have a significant local impact on the chemical weathering reactions taking place in erosion-limited regimes (Cornelis & Delvaux, 2016; Lucas, 2001; Lucas et al., 1993; Meunier et al., 1999).

In summary, the use of Si isotopes and Ge/Si ratios has enabled us to quantify the fate of Si and Ge released via chemical weathering into the proportions that end up either exported in the dissolved phase or sequestered in neoforming clays or plant phytoliths (Table 3). A more traditional approach would require an extensive sampling campaign to quantify these Si pools and their fluxes. Our simple proxy-based calculation allows a first-order estimate of Si and Ge cycle dynamics and can be applied on a range of spatial scales (Baronas et al., 2018). Unavoidably, a number of assumptions underlie this approach, and the results will be sensitive to how well the isotopic or elemental composition of the different pools is represented by sparse sampling. However, all geochemical surveys of natural systems face a similar issue. In fact, in cases where the isotopic composition appears much less variable than the concentration of the element of interest (as is the case with Si in vegetation here: our two plant samples contain very different Si amounts but very similar $\delta^{30}Si_{veg}$ values; Table 1), the isotopic mass budget approach may offer much better precision.

Finally, as noted above, it is important to keep in mind the spatial and temporal scales over which sampling (and mass balance modeling) is undertaken. In our case, the ecosystem impact is clear over timescales relevant to litter senescence, soil-water interaction, and potential topsoil perturbance. Given that we did not establish a mass balance over the full soil thickness down to the bedrock, our model results are not necessarily extendable to geological timescales and long-term export of Si and Ge from the La Selva system. In the following section, we explore what the detrital Ge-Si proxies can reveal about their weathering history on the long timescales over which these signatures are acquired.

4.4. Ge and Si as Tracers of Extreme Weathering in Volcanic Soils

Understanding how the Ge and Si composition of soils and clays encodes information about different weathering processes over the long-term could enable more robust weathering reconstructions using detrital paleorecords. Once continental detritus has been transported and redeposited elsewhere, the absence of parent material makes it difficult to assess the degree of weathering using conventional, element ratio-based proxies such as τ or the Chemical Index of Alteration (CIA; Nesbitt & Young, 1982). The significant advantage of Ge and Si isotope proxies is that primary igneous silicates exhibit only minor variations in their δ^{30}Si and δ^{74}Ge compositions (Escoube et al., 2012; Frings et al., 2016; Savage et al., 2013; Rouxel & Luais, 2017). During chemical weathering, the preferential retention of Ge and light Si isotopes in secondary phases

results in progressively higher Ge/Si and lower δ^{30}Si compositions with increasing weathering intensity (e.g., Cornelis et al., 2014, 2019; Kurtz et al., 2002; Opfergelt & Delmelle, 2012). Our results show that δ^{74}Ge signatures behave similarly, with the soils studied here representing the extreme end of this trend, revealing some of the lowest δ^{30}Si and δ^{74}Ge values measured to date (cf. Baronas et al., 2018; Frings et al., 2016; Rouxel & Luais, 2017; Qi et al., 2019).

To assess more broadly how chemical weathering processes are reflected in the Ge/Si, δ^{30}Si, and δ^{74}Ge signatures of solids, we have compared our La Selva data with a compilation of previously published values for other volcanic soils in tropical areas (Figure 5). The positive correlation between δ^{30}Si and τ_{Si} indicates that soil Si isotopes, to a first order, reflect the degree of Si loss from soils in a relatively linear fashion, reaching a maximum depletion between −2 and −3‰ as τ_{Si} approaches −1 (Figure 5e). Nevertheless, the lighter isotopic composition of clays compared to bulk soils at La Selva demonstrates that additional Si isotopic fractionation can also take place without significant elemental Si depletion.

Similarly, δ^{74}Ge shows strong linear correlation with τ_{Ge} (Figure 5a), consistent with the loss of isotopically heavy dissolved Ge (this study and Baronas et al., 2017, 2018). In contrast to δ^{30}Si, δ^{74}Ge signatures of neoformed clays are indistinguishable from bulk soil, which is consistent with the fact that almost all Ge released during chemical weathering is retained in these phases (f_{sec}Ge = 91 ± 9%, see section 4.3.1). Similar distinction between Ge and Si behavior was already noted using the dissolved and suspended sediment composition of Peruvian rivers (Baronas et al., 2018). As a result, even though both elements exhibit inherent fractionation factors of similar magnitude, secondary weathering phases exhibit a lower degree of fractionation with regard to δ^{74}Ge. Germanium can exhibit siderophile behavior, and incorporation of Ge into Fe oxides can result in isotopic fractionation in the laboratory (Pokrovsky et al., 2014), in marine sediments (Baronas et al., 2019), and potentially during continental weathering (Baronas et al., 2018). While lower δ^{74}Ge values appear to be associated with slightly higher τ_{Fe} in volcanic soils, this relationship is too weak to suggest a mechanistic control of δ^{74}Ge by Fe oxides (Figure 5c). Similarly, Kurtz et al. (2002) noted that Fe does not appear to control Ge/Si fractionation in Hawaiian soils, which is further supported by additional data in this and other recent studies (Figure 5d). Instead, it appears that Ge/Si fractionation in volcanic soils is primarily driven by the preferential loss of Si, rather than the enrichment of Ge (Figures 5b and 5f).

These findings have important implications for the potential use of Si and Ge isotopes as tracers of chemical weathering intensity in detrital paleorecords. Due to the high affinity of Ge to secondary phases, the δ^{74}Ge composition of detrital material will be less sensitive to weathering compared to δ^{30}Si. Based on the Ge isotope dynamics established here, we would expect to find significantly lower δ^{74}Ge, below −0.5 ‰, only in even more extremely weathered soils than those studied here, such as those developed on the oldest Hawaiian island Kauai, which have been shown to exhibit τ_{Ge} close to −1 (Kurtz et al., 2002). If this hypothesis is correct, detrital δ^{74}Ge records could conceivably help reconstruct weathering intensity during some of the hottest periods in Earth's history, such as the early Eocene (Zachos et al., 2001), further improving our understanding of the links between tectonics, weathering, and climate.

5. Conclusions

In this study, we used the distribution of Ge/Si and Ge and Si isotope ratios in the tropical forest soils and waters of La Selva Biological Station, Costa Rica (Figure 1), to better understand the biogeochemical cycling of these elements during the intense weathering of volcanic rocks. The studied soils are depleted of major cations and composed almost entirely of secondary aluminosilicate and oxide phases which are uniformly enriched in Ge/Si and light Ge and Si isotopes relative to the parent rock (Figure 3). The chemical and isotopic composition of investigated streams is highly variable and derives from the mixing of two distinct types of fluids (Figure 4): (1) local soil waters reflecting weathering of the depleted lowland soils and (2) solute-rich interbasin groundwater (IBGW) derived from higher elevations and reflecting the weathering of fresh volcanic rock, as observed by previous researchers (e.g., Genereux et al., 2009; Pringle, 1991). In both cases, weathering produces fluids that have higher δ^{74}Ge and δ^{30}Si and lower Ge/Si than the weathering source substrate, consistent with previous studies on Ge and Si fractionation. The derived fractionation factors were similar in both environments: $\Delta^{30}Si_{sec-diss} = -1.2 \pm 0.1$‰ and -1.7 ± 0.5‰ for the weathering of volcanic rock by IBGW and for the weathering of lowland soils, respectively. The equivalent Ge isotope fractionation

factors were $\Delta^{74}Ge_{sec-diss} = -3.0 \pm 0.9‰$ for IBGW and $-2.3 \pm 0.2‰$ for lowland soils. Reactive transport modeling suggests that IBGW fluids have likely reached chemical and isotopic equilibrium with volcanic rock and precipitating secondary phases. It is notable that the Si and Ge isotope fractionation factors appear to remain relatively constant even in extremely weathered systems, with an isotopic shift of all reservoirs driven by a continuous loss of heavier isotopes in dissolved form. The measured Ge and Si isotope signatures and fractionation factors are summarized in Figure S7.

We used a simple mass balance modeling approach (Baronas et al., 2018) to show that $91 \pm 9\%$ of Ge released via chemical weathering of lowland soils is sequestered by neoforming Al-Si clays, $9 \pm 9\%$ is taken up by vegetation, and only $0.2 \pm 0.2\%$ remains dissolved in the soil pore waters. In contrast, $61 \pm 14\%$ of Si is sequestered by neoforming clays, $39 \pm 14\%$ by vegetation, and $0.5 \pm 0.4\%$ remains as dissolved silica (Table 3). This may indicate that, on the one hand, some Si is being actively accumulated in plant phytoliths, either in the soils or in standing vegetation. On the other hand, the supply of soluble amorphous Si via litterfall enhances clay neoformation in the upper soils, driving the continued fractionation of δ^{30}Si signatures. These results highlight the important role that biological Si cycling can play in tropical ecosystems sustained by highly weathered soils.

Finally, we compiled a number of previous studies of tropical volcanic soils (Bern et al., 2010; Kurtz et al., 2002; Opfergelt et al., 2012; Qi et al., 2019) to identify the first-order controls on δ^{74}Ge, δ^{30}Si, and Ge/Si signatures in solid weathering products (Figure 5). We show that globally, soil δ^{74}Ge closely tracks the depletion of Ge by chemical weathering (τ_{Ge}), whereas δ^{30}Si and Ge/Si both reflect the loss of Si (τ_{Si}). Because Ge is more efficiently retained in solid weathering products than Si, and because Ge and Si isotope signatures reflect the relative mobility of each element, a δ^{74}Ge-δ^{30}Si multiproxy system is sensitive to a wider range of weathering intensities than each isotopic system in isolation. In particular, we hypothesize that solid weathering products with $\delta^{74}Ge < -0.5$ ‰ could be indicative of extremely high weathering intensity environments, where hot and humid conditions are combined with very limited erosion.

Data Availability Statement

All data discussed in this study are publicly available on the HydroShare repository at https://doi.org/10.4211/hs.891fcba010e6490caa614a39d53dccec.

Acknowledgments

This work was financially supported by the UK Natural Environment Research Council (NERC grant NE/H012656/1 to AJW and KWB) and US National Science Foundation (NSF grants OCE-1061700 and OCE-1260692 to DEH and EAR-1455352 to AJW). J. J. B. was additionally supported by the John Montagne Award (Quaternary Geology & Geomorphology Division, GSA) and the InterRidge Research Fellowship. Support for S. O. was provided by the Fonds National de la Recherche Scientifique (FNRS FC69480), Belgium. O. R. was supported by the Institut Carnot Ifremer EDROME and the LabexMer ANR-10-LABX-19-01. Field work was hosted by the Institute of Tropical Studies, La Selva Research Station. We thank Emmanuel Ponzavera for assisting with Ge isotope analyses at Ifremer.

Two anonymous reviewers and the handling editor Peter Raymond are thanked for constructive comments that helped improve the manuscript.

References

Abraham, K., Opfergelt, S., Fripiat, F. A., Cavagna, A. J., de Jong, J. T. M., Foley, S. F., et al. (2008). δ^{30}Si and δ^{29}Si Determinations on USGS BHVO-1 and BHVO-2 Reference Materials with a New Configuration on a Nu Plasma Multi-Collector ICP-MS. *Geostandards and Geoanalytical Research*, *32*(2), 193–202. https://doi.org/10.1111/j.1751-908X.2008.00879.x

Alvarado Induni, G. E. (1990). Caracteristicas geologicas de la Estacion Biologica La Selva. *Tecnologia en Marcha*, *10*(3), 11–22.

Amundson, R. (2013). Soil Formation, (2nd ed.)., *Treatise on geochemistry: Second edition* (Vol. 7, pp. 1–26). Elsevier Ltd. https://doi.org/10.1016/B978-0-08-095975-7.00501-5

Anders, A. M., Sletten, R. S., Derry, L. A., & Hallet, B. (2003). Germanium/silicon ratios in the Copper River Basin, Alaska: Weathering and partitioning in periglacial versus glacial environments. *Journal of Geophysical Research*, *108*(F1), 6005. https://doi.org/10.1029/2003JF000026

Baronas, J. J., Hammond, D. E., Berelson, W. M., McManus, J., & Severmann, S. (2016). Germanium-silicon fractionation in a river-influenced continental margin: The Northern Gulf of Mexico. *Geochimica et Cosmochimica Acta*, *178*, 124–142. https://doi.org/10.1016/j.gca.2016.01.028

Baronas, J. J., Hammond, D. E., McManus, J., Wheat, C. G., & Siebert, C. (2017). A global Ge isotope budget. *Geochimica et Cosmochimica Acta*, *203*, 265–283. https://doi.org/10.1016/j.gca.2017.01.008

Baronas, J. J., Hammond, D. E., Rouxel, O. J., & Monteverde, D. R. (2019). A first look at dissolved Ge isotopes in marine sediments. *Frontiers in Earth Science*, *7*(June), 1–17. https://doi.org/10.3389/feart.2019.00162

Baronas, J. J., Torres, M. A., West, A. J., Rouxel, O. J., Georg, R. B., Bouchez, J., et al. (2018). Ge and Si isotope signatures in rivers: A quantitative multi-proxy approach. *Earth and Planetary Science Letters*, *503*, 194–215. https://doi.org/10.1016/j.epsl.2018.09.022

Bern, C. R., Brzezinski, M., Beucher, C., Ziegler, K., & Chadwick, O. (2010). Weathering, dust, and biocycling effects on soil silicon isotope ratios. *Geochimica et Cosmochimica Acta*, *74*(3), 876–889. https://doi.org/10.1016/j.gca.2009.10.046

Berner, R. A., Lasaga, A. C., & Garrels, R. M. (1983). The carbonate-silicate geochemical cycle and its effect on atmospheric carbon dioxide over the past 100 million years. *American Journal of Science*, *283*, 641–683.

Bernstein, L. R. (1985). Germanium geochemistry and mineralogy. *Geochimica et Cosmochimica Acta*, *49*, 2409–2422.

Blanchard, M., Balan, E., & Schauble, E. A. (2017). Equilibrium fractionation of non-traditional isotopes: A molecular modeling perspective. *Reviews in Mineralogy and Geochemistry*, *82*(1), 27–63. https://doi.org/10.2138/rmg.2017.82.2

Blecker, S. W., King, S. L., Derry, L. A., Chadwick, O. A., Ippolito, J. A., & Kelly, E. F. (2007). The ratio of germanium to silicon in plant phytoliths: Quantification of biological discrimination under controlled experimental conditions. *Biogeochemistry*, *86*(2), 189–199. https://doi.org/10.1007/s10533-007-9154-7

Bouchez, J., von Blanckenburg, F., & Schuessler, J. A. (2013). Modeling novel stable isotope ratios in the weathering zone. *American Journal of Science*, *313*(4), 267–308. https://doi.org/10.2475/04.2013.01

Brantley, S., Kubicki, J. D., & White, A. F. (2008). *Kinetics of water-rock interaction Edited by* Brantley, S. L., Kubicki, J. D., & White, A. F. New York: Springer.

Brimhall, G. H., & Dietrich, W. E. (1987). Constitutive mass balance relations between chemical composition, volume, density, porosity, and strain in metasomatic hydrochemical systems: Results on weathering and pedogenesis. *Geochimica et Cosmochimica Acta*, *51*(3), 567–587.

Chadwick, O. A., Brimhall, G. H., & Hendricks, D. M. (1990). From a black to a gray box—A mass balance interpretation of pedogenesis. *Geomorphology*, *3*(3-4), 369–390. https://doi.org/10.1016/0169-555X(90)90012-F

Chapela Lara, M. A., Buss, H. L., Pogge von Strandmann, P. A. E., Schuessler, J. A., & Moore, O. W. (2017). The influence of critical zone processes on the Mg isotope budget in a tropical, highly weathered andesitic catchment. *Geochimica et Cosmochimica Acta*, *202*, 77–100. https://doi.org/10.1016/j.gca.2016.12.032

Clark, D. B., & Clark, D. A. (2000). Landscape-scale variation in forest structure and biomass in a tropical rain forest. *Forest Ecology and Management*, *137*(1-3), 185–198. https://doi.org/10.1016/S0378-1127(99)00327-8

Clarke, J. (2003). The occurrence and significance of biogenic opal in the regolith. *Earth-Science Reviews*, *60*(3-4), 175–194. https://doi.org/10.1016/S0012-8252(02)00092-2

Cornelis, J.-T., & Delvaux, B. (2016). Soil processes drive the biological silicon feedback loop. *Functional Ecology*, *30*(8), 1298–1310. https://doi.org/10.1111/1365-2435.12704

Cornelis, J.-T., Delvaux, B., Cardinal, D., André, L., Ranger, J., & Opfergelt, S. (2010). Tracing mechanisms controlling the release of dissolved silicon in forest soil solutions using Si isotopes and Ge/Si ratios. *Geochimica et Cosmochimica Acta*, *74*(14), 3913–3924. https://doi.org/10.1016/j.gca.2010.04.056

Cornelis, J.-T., Weis, D., Lavkulich, L., Vermeire, ML., Delvaux, B., & Barling, J. (2014). Silicon isotopes record dissolution and re-precipitation of pedogenic clay minerals in a podzolic soil chronosequence. *Geoderma*, *235-236*, 19–29. https://doi.org/10.1016/j.geoderma.2014.06.023

Cornelis, J.-T., Weis, D., Opfergelt, S., Van Ranst, E., & Dumon, M. (2019). Past and current geochemical conditions influence silicon isotope signatures of pedogenic clay minerals at the soil profile scale, Ethiopia. *Chemical Geology*, *524*(June), 174–183. https://doi.org/10.1016/j.chemgeo.2019.06.013

De Argollo, R., & Schilling, J.-G. (1978). Ge-Si and Ga-Al fractionation in Hawaiian volcanic rocks. *Geochimica et Cosmochimica Acta*, *42*(6), 623–630. https://doi.org/10.1016/0016-7037(78)90007-8

Dellinger, M., Gaillardet, J., Bouchez, J., Calmels, D., Louvat, P., Dosseto, A., et al. (2015). Riverine Li isotope fractionation in the Amazon River basin controlled by the weathering regimes. *Geochimica et Cosmochimica Acta*, *164*, 71–93. https://doi.org/10.1016/j.gca.2015.04.042

Delstanche, S., Opfergelt, S., Cardinal, D., Elsass, F., André, L., & Delvaux, B. (2009). Silicon isotopic fractionation during adsorption of aqueous monosilicic acid onto iron oxide. *Geochimica et Cosmochimica Acta*, *73*(4), 923–934. https://doi.org/10.1016/j.gca.2008.11.014

Delvigne, C., Opfergelt, S., Cardinal, D., Delvaux, B., & André, L. (2009). Distinct silicon and germanium pathways in the soil-plant system: Evidence from banana and horsetail. *Journal of Geophysical Research*, *114*, G02013. https://doi.org/10.1029/2008JG000899

Derry, L. A., Kurtz, A. C., Ziegler, K., & Chadwick, O. A. (2005). Biological control of terrestrial silica cycling and export fluxes to watersheds. *Nature*, *433*, 728–31. https://doi.org/10.1038/nature03299

Ding, T. P., Ma, G. R., Shui, M. X., Wan, D. F., & Li, R. H. (2005). Silicon isotope study on rice plants from the Zhejiang province, China. *Chemical Geology*, *218*(1-2), 41–50. https://doi.org/10.1016/j.chemgeo.2005.01.018

Eklund, T. J., McDowell, W. H., & Pringle, C. M. (1997). Seasonal variation of tropical precipitation chemistry: La Selva, Costa Rica. *Atmospheric Environment*, *31*(23), 3903–3910. https://doi.org/10.1016/S1352-2310(97)00246-X

Escoube, R., Rouxel, O. J., Edwards, K., Glazer, B., & Donard, O. F. X. (2015). Coupled Ge/Si and Ge isotope ratios as geochemical tracers of seafloor hydrothermal systems: Case studies at Loihi Seamount and East Pacific Rise 9°50′N. *Geochimica et Cosmochimica Acta*, *167*, 93–112. https://doi.org/10.1016/j.gca.2015.06.025

Escoube, R., Rouxel, O. J., Luais, B. A., Ponzevera, E., & Donard, O. F. X. (2012). An intercomparison study of the germanium isotope composition of geological reference materials. *Geostandards and Geoanalytical Research*, *36*(2), 149–159. https://doi.org/10.1111/j.1751-908X.2011.00135.x

Fernandez, N. M., Zhang, X., & Druhan, J. L. (2019). Silicon isotopic re-equilibration during amorphous silica precipitation and implications for isotopic signatures in geochemical proxies. *Geochimica et Cosmochimica Acta*, *262*, 104–127. https://doi.org/10.1016/j.gca.2019.07.029

Frings, P. J., & Buss, H. L. (2019). The central role of weathering in the geosciences. *Elements*, *15*(4), 229–234. https://doi.org/10.2138/gselements.15.4.229

Frings, P. J., Clymans, W., Fontorbe, G., De La Rocha, C. L., & Conley, D. J. (2016). The continental Si cycle and its impact on the ocean Si isotope budget. *Chemical Geology*, *425*, 12–36. https://doi.org/10.1016/j.chemgeo.2016.01.020

Froelich, P. N., Blanc, V., Mortlock, R. A., Chillrud, S. N., Dunstan, W., Udomkit, A., & Peng, T. H. (1992). River fluxes of dissolved silica to the ocean were higher during glacials: Ge/Si in diatoms, rivers, and oceans. *Paleoceanography*, *7*(6), 739–767.

Froelich, P. N., Hambrick, G. A., Andreae, M. O., Mortlock, R. A., & Edmond, J. M. (1985). The geochemistry of inorganic germanium in natural waters. *Journal of Geophysical Research*, *90*(C1), 1133–1141.

Gaillardet, J. A. A. B., Dupré, B., & Allègre, C. J. (1995). A global geochemical mass budget applied to the Congo basin rivers: Erosion rates and continental crust composition. *Geochimica et Cosmochimica Acta*, *59*(17), 3469–3485. https://doi.org/10.1016/0016- 7037(95)00230-W

Genereux, D. P. (2004). Comparison of naturally-occurring chloride and oxygen-18 as tracers of interbasin groundwater transfer in lowland rainforest, Costa Rica. *Journal of Hydrology*, *295*, 17–27. https://doi.org/10.1016/j.jhydrol.2004.02.020

Genereux, D. P., & Jordan, M. (2006). Interbasin groundwater flow and groundwater interaction with surface water in a lowland rainforest, Costa Rica: A review. *Journal of Hydrology*, *320*(3-4), 385–399. https://doi.org/10.1016/j.jhydrol.2005.07.023

Genereux, D. P., Jordan, M. T., & Carbonell, D. (2005). A paired-watershed budget study to quantify interbasin groundwater flow in a lowland rain forest, Costa Rica. *Water Resources Research*, *41*, W04011. https://doi.org/10.1029/2004WR003635

Genereux, D. P., & Pringle, C. (1997). Chemical mixing model of streamflow generation at La Selva Biological Station, Costa Rica. *Journal of Hydrology*, *199*(3-4), 319–330. https://doi.org/10.1016/S0022-1694(96)03333-1

Genereux, D. P., Webb, M., & Solomon, D. K. (2009). Chemical and isotopic signature of old groundwater and magmatic solutes in a Costa Rican rain forest: Evidence from carbon, helium, and chlorine. *Water Resources Research*, *45*, W08413. https://doi.org/10.1029/2008WR007630

Genereux, D. P., Wood, S. J., & Pringle, C. M. (2002). Chemical tracing of interbasin groundwater transfer in the lowlandrainforest of Costa Rica. *Journal of Hydrology*, *258*, 163–178. https://doi.org/10.1016/S0022-1694(01)00568-6

Georg, R. B., Reynolds, B. C., Frank, M., & Halliday, A. N. (2006a). Mechanisms controlling the silicon isotopic compositions of river waters. *Earth and Planetary Science Letters*, *249*(3-4), 290–306. https://doi.org/10.1016/j.epsl.2006.07.006

Georg, R. B., Reynolds, B. C., Frank, M., & Halliday, A. N. (2006b). New sample preparation techniques for the determination of Si isotopic compositions using MC-ICPMS. *Chemical Geology*, *235*(1-2), 95–104. https://doi.org/10.1016/j.chemgeo.2006.06.006

Georg, R. B., Reynolds, B. C., West, A. J., Burton, K. W., & Halliday, A. N. (2007). Silicon isotope variations accompanying basalt weathering in Iceland. *Earth and Planetary Science Letters*, *261*(3-4), 476–490. https://doi.org/10.1016/j.epsl.2007.07.004

Georg, R. B., West, A. J., Basu, A. R., & Halliday, A. N. (2009). Silicon fluxes and isotope composition of direct groundwater discharge into the Bay of Bengal and the effect on the global ocean silicon isotope budget. *Earth and Planetary Science Letters*, *283*(1-4), 67–74. https://doi.org/10.1016/j.epsl.2009.03.041

Georg, R. B., Zhu, C., Reynolds, B. C., & Halliday, A. N. (2009). Stable silicon isotopes of groundwater, feldspars, and clay coatings in the Navajo Sandstone aquifer, Black Mesa, Arizona, USA. *Geochimica et Cosmochimica Acta*, *73*(8), 2229–2241. https://doi.org/10.1016/j.gca.2009.02.005

Guillermic, M., Lalonde, S. V., Hendry, K. R., & Rouxel, O. J. (2017). The isotope composition of inorganic germanium in seawater and deep sea sponges. *Geochimica et Cosmochimica Acta*, *212*, 99–118. https://doi.org/10.1016/j.gca.2017.06.011

Hammond, D. E., McManus, J., & Berelson, W. M. (2004). Oceanic germanium/silicon ratios: Evaluation of the potential overprint of temperature on weathering signals. *Paleoceanography*, *19*, PA2016. https://doi.org/10.1029/2003PA000940

Hathorne, E. C., & James, R. H. (2006). Temporal record of lithium in seawater: A tracer for silicate weathering?. *Earth and Planetary Science Letters*, *246*(3-4), 393–406. https://doi.org/10.1016/j.epsl.2006.04.020

Hodson, M. J., White, P. J., Mead, A., & Broadley, M. R. (2005). Phylogenetic variation in the silicon composition of plants. *Annals of Botany*, *96*(6), 1027–1046. https://doi.org/10.1093/aob/mci255

Hughes, H. J., Sondag, F., Santos, R. V., André, L., & Cardinal, D. (2013). The riverine silicon isotope composition of the Amazon Basin. *Geochimica et Cosmochimica Acta*, *121*, 637–651. https://doi.org/10.1016/j.gca.2013.07.040

Johnson, C. M., Beard, B. L., & Albarede, F. (2004). Overview and general concepts. *Reviews in Mineralogy and Geochemistry*, *55*(1), 1–24. https://doi.org/10.2138/gsrmg.55.1.1

Kautz, C. Q., & Ryan, P. C. (2003). The 10 A to 7 A halloysite transition in a tropical soil sequence, Costa Rica. *Clays and Clay Minerals*, *51*(3), 252–263. https://doi.org/10.1346/CCMN.2003.0510302

Kleber, M., Schwendenmann, L., Veldkamp, E., Rößner, J., & Jahn, R. (2007). Halloysite versus gibbsite: Silicon cycling as a pedogenetic process in two lowland neotropical rain forest soils of La Selva, Costa Rica. *Geoderma*, *138*(1-2), 1–11. https://doi.org/10.1016/j.geoderma.2006.10.004

Kurtz, A. C., Derry, L. A., & Chadwick, O. A. (2002). Germanium-silicon fractionation in the weathering environment. *Geochimica et Cosmochimica Acta*, *66*(9), 1525–1537.

Kurtz, A. C., Lugolobi, F., & Salvucci, G. (2011). Germanium-silicon as a flow path tracer: Application to the Rio Icacos watershed. *Water Resources Research*, *47*, W06516. https://doi.org/10.1029/2010WR009853

Li, Z., Cornelis, J.-T., Vander Linden, C., Ranst, E. V., & Delvaux, B. (2020). Neoformed aluminosilicate and phytogenic silica are competitive sinks in the silicon soil plant cycle. *Geoderma*, *368*(January), 114308. https://doi.org/10.1016/j.geoderma.2020.114308

Li, Z., de Tombeur, F. A., Vander Linden, C., Cornelis, J. T., & Delvaux, B. (2020). Soil microaggregates store phytoliths in a sandy loam. *Geoderma*, *360*(October 2019), 114,037. https://doi.org/10.1016/j.geoderma.2019.114037

Li, G., & Elderfield, H. (2013). Evolution of carbon cycle over the past 100 million years. *Geochimica et Cosmochimica Acta*, *103*, 11–25. https://doi.org/10.1016/j.gca.2012.10.014

Li, G., & West, A. J. (2014). Evolution of Cenozoic seawater lithium isotopes: Coupling of global denudation regime and shifting seawater sinks. *Earth and Planetary Science Letters*, *401*, 284–293. https://doi.org/10.1016/j.epsl.2014.06.011

Lucas, Y. (2001). The role of plants in controlling rates and products of weathering: Importance of biological pumping. *Annual Review of Earth and Planetary Sciences*, *29*(1), 135–163. https://doi.org/10.1146/annurev.earth.29.1.135

Lucas, Y., Luizao, F. J., Chauvel, A., Rouiller, J., & Nahon, D. (1993). The relation between biological activity of the rain forest and mineral composition of soils. *Science*, *260*(5107), 521–523. https://doi.org/10.1126/science.260.5107.521

Lugolobi, F., Kurtz, A. C., & Derry, L. A. (2010). Germanium-silicon fractionation in a tropical, granitic weathering environment. *Geochimica et Cosmochimica Acta*, *74*(4), 1294–1308. https://doi.org/10.1016/j.gca.2009.11.027

Macdonald, F. A., Swanson-Hysell, N. L., Park, Y., Lisiecki, L., & Jagoutz, O. (2019). Arc-continent collisions in the tropics set Earth's climate state. *Science*, *5300*(March), 1–12.

McDade, L. A., Bawa, K. S., Hespenheide, H. A., & Hartshorn, G. S. (1994a). *La Selva: Ecology and natural history of a neotropical rain forest*: University of Chicago Press.

McDade, L. A., Bawa, K. S., Hespenheide, H. A., & Hartshorn, G. S. (1994b). Vegetation types and floristic patterns. In L. A. McDade, K. S. Bawa, H. A. Hespenheide, & G. S. Hartshorn (Eds.), *La Selva: Ecology and natural history of a neotropical rain forest* (pp. 73–89): The University of Chicago Press. https://doi.org/10.2307/5839

Meek, K., Derry, L., Sparks, J., & Cathles, L. (2016). 87Sr/86Sr, Ca/Sr, and Ge/Si ratios as tracers of solute sources and biogeochemical cycling at a temperate forested shale catchment, central Pennsylvania, USA. *Chemical Geology*, *445*, 84–102. https://doi.org/10.1016/j.chemgeo.2016.04.026

Meunier, J. D., Colin, F., & Alarcon, C. (1999). Biogenic silica storage in soils. *Geology*, *27*(9), 835–838.

Misra, S., & Froelich, P. N. (2012). Lithium isotope history of Cenozoic seawater: Changes in silicate weathering and reverse weathering. *Science*, *335*(6070), 818–823. https://doi.org/10.1126/science.1214697

Mortlock, R. A., & Froelich, P. N. (1987). Continental weathering of germanium: Ge/Si in the global river discharge. *Geochimica et Cosmochimica Acta*, *51*, 2075–2082.

Mortlock, R. A., & Froelich, P. N. (1996). Determination of germanium by isotope dilution-hydride generation inductively coupled plasma mass spectrometry. *Analytica Chimica Acta*, *332*, 277–284.

Murnane, R. J., & Stallard, R. F. (1990). Germanium and silicon in rivers of the Orinoco drainage basin. *Nature*, *344*, 749–752.

Nesbitt, H. W. (1979). Mobility and fractionation of REE during weathering of a granodiorite. *Nature*, *279*, 206–210.

Nesbitt, H. W., & Young, G. M. (1982). Early Proterozoic climates and plate motions inferred from major element chemistry of lutites. *Nature*, *299*(5885), 715–717. https://doi.org/10.1038/299715a0

Oelze, M., von Blanckenburg, F., Bouchez, J., Hoellen, D., & Dietzel, M. (2015). The effect of Al on Si isotope fractionation investigated by silica precipitation experiments. *Chemical Geology*, *397*, 94–105. https://doi.org/10.1016/j.chemgeo.2015.01.002

Oelze, M., von Blanckenburg, F., Hoellen, D., Dietzel, M., & Bouchez, J. (2014). Si stable isotope fractionation during adsorption and the competition between kinetic and equilibrium isotope fractionation: Implications for weathering systems. *Chemical Geology*, *380*, 161–171. https://doi.org/10.1016/j.chemgeo.2014.04.027

Opfergelt, S., Cardinal, D., André, L., Delvigne, C., Bremond, L., & Delvaux, B. (2010). Variations of δ30Si and Ge/Si with weathering and biogenic input in tropical basaltic ash soils under monoculture. *Geochimica et Cosmochimica Acta*, *74*(1), 225–240. https://doi.org/10.1016/j.gca.2009.09.025

Opfergelt, S., Cardinal, D., Henriet, C., Draye, X., André, L., & Delvaux, B. (2006). Silicon isotopic fractionation by banana (Musa spp.) grown in a continuous nutrient flow device. *Plant and Soil*, *285*(1-2), 333–345. https://doi.org/10.1007/s11104-006-9019-1

Opfergelt, S., & Delmelle, P. (2012). Silicon isotopes and continental weathering processes: Assessing controls on Si transfer to the ocean. *Comptes Rendus - Geoscience*, *344*(11-12), 723–738. https://doi.org/10.1016/j.crte.2012.09.006

Opfergelt, S., Georg, R. B., Delvaux, B., Cabidoche, Y.-M., Burton, K. W., & Halliday, A. N. (2012). Silicon isotopes and the tracing of desilication in volcanic soil weathering sequences, Guadeloupe. *Chemical Geology*, *326-327*, 113–122. https://doi.org/10.1016/j.chemgeo.2012.07.032

Parfitt, R. L., & Childs, C. W. (1988). Estimation of forms of Fe and Al—A review, and analysis of contrasting soils by dissolution and Mossbauer methods. *Soil Research*, *26*(1), 121. https://doi.org/10.1071/SR9880121

Pogge von Strandmann, P. A. E., & Henderson, G. M. (2015). The Li isotope response to mountain uplift. *Geology*, *43*(1), 67–70. https://doi.org/10.1130/G36162.1

Pogge von Strandmann, P. A. E., Porcelli, D., James, R. H., van Calsteren, P., Schaefer, B., Cartwright, I., et al. (2014). Chemical weathering processes in the Great Artesian Basin: Evidence from lithium and silicon isotopes. *Earth and Planetary Science Letters*, *406*, 24–36. https://doi.org/10.1016/j.epsl.2014.09.014

Pokrovsky, O. S., Galy, A., Schott, J., Pokrovski, G. S., & Mantoura, S. (2014). Germanium isotope fractionation during Ge adsorption on goethite and its coprecipitation with Fe oxy(hydr)oxides. *Geochimica et Cosmochimica Acta*, *131*, 138–149. https://doi.org/10.1016/j.gca.2014.01.023

Porcelli, D. (2008). Chapter 4 Investigating Groundwater Processes Using U- and Th-Series Nuclides. *Radioactivity in the Environment*, *13*(7), 105–153. https://doi.org/10.1016/S1569-4860(07)00004-6

Porder, S., Clark, D. A., & Vitousek, P. M. (2006). Persistence of rock-derived nutrients in the wet tropical forests of La Selva, Costa Rica. *Ecology*, *87*(3), 594–602. https://doi.org/10.1890/05-0394

Pringle, C. M. (1991). Geothermally modified waters surface at La Selva Biological Station, Costa Rica: Volcanic processes introduce chemical discontinuities into lowland tropical streams. *Biotropica*, *23*(4), 523–529.

Pringle, C. M., Triska, F. J., & Browder, G. (1990). Spatial variation in basic chemistry of streams draining a volcanic landscape on Costa Rica's Caribbean slope. *Hydrobiologia*, *206*, 73–85.

Qi, H. W., Hu, R. Z., Jiang, K., Zhou, T., Liu, Y. F., & Xiong, Y. W. (2019). Germanium isotopes and Ge/Si fractionation under extreme tropical weathering of basalts from the Hainan Island, South China. *Geochimica et Cosmochimica Acta*, *253*, 249–266. https://doi.org/10.1016/j.gca.2019.03.022

Raymo, M. E., & Ruddiman, W. F. (1992). Tectonic forcing of late Cenozoic climate. *Nature*, *359*(6391), 117–122. https://doi.org/10.1038/359117a0

Reynolds, B. C., Aggarwal, J., Brzezinski, M., Cardinal, D., Engstrom, E., Georg, R. B., et al. (2007). An inter-laboratory comparison of Si isotope reference materials. *Journal of Analytical Atomic Spectrometry*, *22*, 561–568. https://doi.org/10.1039/b616755a

Roerdink, D. L., van den Boorn, S. H., Geilert, S., Vroon, P. Z., & van Bergen, M. J. (2015). Experimental constraints on kinetic and equilibrium silicon isotope fractionation during the formation of non-biogenic chert deposits. *Chemical Geology*, *402*, 40–51. https://doi.org/10.1016/j.chemgeo.2015.02.038

Rouxel, O. J., Galy, A., & Elderfield, H. (2006). Germanium isotopic variations in igneous rocks and marine sediments. *Geochimica et Cosmochimica Acta*, *70*(13), 3387–3400. https://doi.org/10.1016/j.gca.2006.04.025

Rouxel, O. J., & Luais, B. A. (2017). Germanium isotope geochemistry. *Reviews in Mineralogy and Geochemistry*, *82*(1), 601–656. https://doi.org/10.2138/rmg.2017.82.14

Sanford, R. L. J., Paaby, P., Luvall, J. C., & Phillips, E. (1994). Climate, geomorphology, and aquatic systems, *La Selva: Ecology and Natural History of a Tropical Rainforest* (pp. 19–33). University of Chicago Press Chicago.

Savage, P. S., Georg, R. B., Williams, H. M., & Halliday, A. N. (2013). The silicon isotope composition of the upper continental crust. *Geochimica et Cosmochimica Acta*, *109*, 384–399. https://doi.org/10.1016/j.gca.2013.02.004

Schott, J., Pokrovsky, O. S., & Oelkers, E. H. (2009). The link between mineral dissolution/precipitation kinetics and solution chemistry. *Reviews in Mineralogy and Geochemistry*, *70*(1), 207–258. https://doi.org/10.2138/rmg.2009.70.6

Schuessler, J. A., von Blanckenburg, F., Bouchez, J., Uhlig, D., & Hewawasam, T. (2018). Nutrient cycling in a tropical montane rainforest under a supply-limited weathering regime traced by elemental mass balances and Mg stable isotopes. *Chemical Geology*, *497*(August), 74–87. https://doi.org/10.1016/j.chemgeo.2018.08.024

Siebert, C., Nägler, T. F., & Kramers, J. D. (2001). Determination of molybdenum isotope fractionation by double-spike multicollector inductively coupled plasma mass spectrometry. *Geochemistry Geophysics Geosystems*, *2*, 1032.

Sollins, P., Sancho M., F., Mata Ch., R., & Sanford Jr, R. L. (1994). Soils and soil process research, *La Selva: Ecology and natural history of a tropical rainforest* (pp. 34–53). University of Chicago Press.

Song, Z., McGrouther, K., & Wang, H. (2016). Occurrence, turnover and carbon sequestration potential of phytoliths in terrestrial ecosystems. *Earth-Science Reviews*, *158*(92), 19–30. https://doi.org/10.1016/j.earscirev.2016.04.007

Song, Z., Wang, H., Strong, P. J., Li, Z., & Jiang, P. (2012). Plant impact on the coupled terrestrial biogeochemical cycles of silicon and carbon: Implications for biogeochemical carbon sequestration. *Earth-Science Reviews*, *115*(4), 319–331. https://doi.org/10.1016/j.earscirev.2012.09.006

Sparks, J. P., Chandra, S., Derry, L., Parthasarathy, M. V., Daugherty, C. S., & Griffin, R. (2010). Subcellular localization of silicon and germanium in grass root and leaf tissues by SIMS: Evidence for differential and active transport. *Biogeochemistry*, *104*(1-3), 237–249. https://doi.org/10.1007/s10533-010-9498-2

Stallard, R. F., & Edmond, J. M. (1983). Geochemistry of the Amazon: 2. The influence of geology and weathering environment on the dissolved load. *Journal of Geophysical Research*, *88*, 9671–9688.

Tricca, A., Porcelli, D., & Wasserburg, G. J. (2000). Factors controlling the groundwater transport of U, Th, Ra, and Rn. *Proceedings of the Indian Academy of Sciences, Earth and Planetary Sciences*, *109*(1), 95–108. https://doi.org/10.1007/BF02719153

Uhlig, D., Schuessler, J. A., Bouchez, J., Dixon, J. L., & Von Blanckenburg, F. (2017). Quantifying nutrient uptake as driver of rock weathering in forest ecosystems by magnesium stable isotopes. *Biogeosciences*, *14*(12), 3111–3128. https://doi.org/10.5194/bg-14-3111-2017

Veldkamp, E., Becker, A., Schwendenmann, L., Clark, D. J., & Schulte-Bisping, H. (2003). Substantial labile carbon stocks and microbial activity in deeply weathered soils below a tropical wet forest. *Global Change Biology*, *9*, 1171–1184. https://doi.org/10.1046/j.1365-2486.2003.00656.x

Viers, J., Dupré, B., Braun, J. J., Deberdt, S., Angeletti, B., Ngoupayou, J. N., & Michard, A. (2000). Major and trace element abundances, and strontium isotopes in the Nyong basin rivers (Cameroon): Constraints on chemical weathering processes and elements transport mechanisms in humid tropical environments. *Chemical Geology*, *169*, 211–241. https://doi.org/10.1016/S0009-2541(00)00298-9

Wagai, R., Mayer, L. M., Kitayama, K., & Shirato, Y. (2013). Association of organic matter with iron and aluminum across a range of soils determined via selective dissolution techniques coupled with dissolved nitrogen analysis. *Biogeochemistry*, *112*(1-3), 95–109. https://doi.org/10.1007/s10533-011-9652-5

Walker, J. C., Hays, P. B., & Kasting, J. F. (1981). A negative feedback mechanism for the long-term stabilization of Earth's surface temperature. *Journal of Geophysical Research*, *86*(C10), 9776–9782. https://doi.org/10.1029/JC086iC10p09776

Watkins, J. M., DePaolo, D. J., & Watson, E. B. (2017). Kinetic fractionation of non-traditional stable isotopes by diffusion and crystal growth reactions. *Reviews in Mineralogy and Geochemistry*, *82*(1), 85–125. https://doi.org/10.2138/rmg.2017.82.4

West, A., Galy, A., & Bickle, M. (2005). Tectonic and climatic controls on silicate weathering. *Earth and Planetary Science Letters*, *235*(1-2), 211–228. https://doi.org/10.1016/j.epsl.2005.03.020

White, A. F., Vivit, D. V., Schulz, M. S., Bullen, T. D., Evett, R. R., & Aagarwal, J. (2012). Biogenic and pedogenic controls on Si distributions and cycling in grasslands of the Santa Cruz soil chronosequence, California. *Geochimica et Cosmochimica Acta*, *94*, 72–94. https://doi.org/10.1016/j.gca.2012.06.009

Wiegand, B. a., & Schwendenmann, L. (2013). Determination of Sr and Ca sources in small tropical catchments (La Selva, Costa Rica)—A comparison of Sr and Ca isotopes. *Journal of Hydrology*, *488*, 110–117. https://doi.org/10.1016/j.jhydrol.2013.02.044

Wood, T. E., Lawrence, D., & Clark, D. A. (2006). Determinants of leaf litter nutrient cycling in a tropical rain forest: Soil fertility versus topography. *Ecosystems*, *9*(5), 700–710. https://doi.org/10.1007/s10021-005-0016-7

Zachos, J., Pagani, M., Sloan, L., Thomas, E., & Billups, K. (2001). Trends, rhythms, and aberrations in global climate 65 Ma to present. *Science*, *292*(5517), 686–93. https://doi.org/10.1126/science.1059412

Ziegler, K., Chadwick, O. A., Brzezinski, M. A., & Kelly, E. F. (2005). Natural variations of d30Si ratios during progressive basalt weathering, Hawaiian Islands. *Geochimica et Cosmochimica Acta*, *69*(19), 4597–4610. https://doi.org/10.1016/j.gca.2005.05.008

References From the Supporting Information

Brantley, S., & Olsen, A. A. (2013). Reaction kinetics of primary rock-forming minerals under ambient conditions, (2nd ed.)., *Treatise on geochemistry: Second edition* (Vol. 7, pp. 69–113). Elsevier Ltd. https://doi.org/10.1016/B978-0-08-095975-7.00503-9

Chesworth, W., Dejou, J., & Larroque, P. (1981). The weathering of basalt and relative mobilities of the major elements at Belbex, France. *Geochimica et Cosmochimica Acta*, *45*(7), 1235–1243. https://doi.org/10.1016/0016-7037(81)90147-2

Maher, K., & Chamberlain, C. P. (2014). Hydrologic regulation of chemical weathering and the geologic carbon cycle. *Science*, *343*(6178), 1502–4. https://doi.org/10.1126/science.1250770

Middelburg, J., Weijden, C. V. D., & Woittiez, J. (1988). Chemical processes affecting the mobility of major, minor and trace elements during weathering of granitic rocks. *Chemical Geology*, *68*, 253–273. https://doi.org/10.1016/0009-2541(88)90025-3

Parkhurst, D. L., & Appelo, C. A. J. (2013). Description of input and examples for PHREEQC version 3: A computer program for speciation, batch-reaction, one-dimensional transport, and inverse geochemical calculations: US Geological Survey. https://doi.org/10.3133/tm6A43